Westfälische Wilhelms-Universität Münster

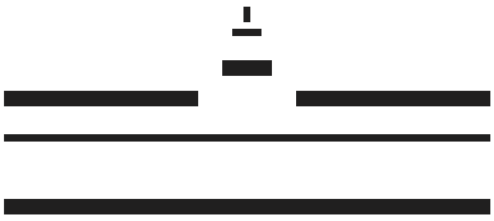

WESTFÄLISCHE
WILHELMS-UNIVERSITÄT
MÜNSTER

MASTER THESIS

The Localized Subtraction Source Model

For Solving the EEG and MEG Forward Problem using the Continuous Galerkin Finite Element Method

Author:

Pia Lange
Matr.: 418662

Supervisors:

Prof. Dr. Christian Engwer
Institute for Applied Mathematics WWU

Prof. Dr. Carsten Wolters
Institute for Biomagnetism and Biosignalanalysis WWU

Date of submission: December 30, 2021

Abstract

This thesis presents the localized subtraction source model, a modification of the subtraction source model. The advantage of the localization is that it results in a sparse right-hand side and therefore profits immensely from using the transfer matrix approach. Originally, the localized subtraction source model was introduced in a DG-FEM framework. A continuous adaptation is proposed and a CG-FEM formulation is derived.
To achieve accurate results for the MEG forward problem, we apply a boundary approach, that was originally designed for the subtraction approach.
For both the EEG and MEG forward problem, the localized subtraction source model accomplishes a major speed up of the computation time while achieving even better accuracy than the subtraction source model.

Contents

1 Introduction

A particular interest of brain research is to reconstruct the location of a neuronal activity. A neuronal activity produces an electric field which in turn causes a magnetic field. The fields can be measured by electroencephalography (EEG) and magnetoencephalography (MEG), respectively.
To solve the inverse problem, that wants to reconstruct the source, we first need to look at the so-called *forward problem*. Here we assume a known source in the brain and aim to calculate the electric and magnetic field that would be produced by this source. In realistic scenarios, these calculations can not be done analytically, but require a numerical approximation.
Naturally, the accuracy of the inverse solution significantly depends on the accuracy of the forward solution. Furthermore, the forward problem has to be solved for many source locations. In realistic head models, this means more than 10^4 forward calculations. Conclusively, time-efficient algorithms and models are needed. Inherently, one often has to sacrifice some accuracy for the sake of saving time or vice versa. There are however strategies, like the *transfer matrix approach* that can immensely cut calculation time without losing any accuracy.
One essential modelling choice in setting up the forward problem is the *source model*, for example the *partial integration*, *Venant* or *subtraction* source model. The latter is the most accurate, in particular when it comes to the MEG problem. However, it does not profit from the transfer matrix approach in the same way as the other models and is therefore heavily outperformed concerning calculation time, making it practically unuseable for realistic applications.
This thesis will present the *localized subtraction* source model, that starts from the same idea as the subtraction source model, but makes better use of the transfer matrix approach. We will evaluate to what extent this variation effects the accuracy of the solution and conclude if it can make the subtraction approach applicable for real life studies. The localized subtraction source model was first proposed by A. Nüßing [8] in a discontinuous Galerkin finite element disretization for the EEG problem. This thesis shows how it can be adapted to fit a conforming discretization and also apply it to the MEG forward problem.
For the subtraction source model, M. C. Piastra [10] suggested a *boundary approach* to calculate the MEG solution, which will also be used for the localized subtraction source model.

This thesis is structured as follows: In chapter 1 the general mathematical models and methods for solving the EEG and MEG forward problem are explained. Chapter 2 introduces the subtraction source model. A continuous Galerkin formulation to obtain a numerical solution is given. For the MEG problem, the boundary approach is derived. Chapter 3 is about the localized subtraction source model. It is introduced in its original discontinuous formulation and then adapted for the continuous Galerkin method. Furthermore, the boundary approach is applied for solving the MEG forward problem. In chapter 5 results of numerical experiments in a spherical head model are shown. The localized subtraction source model is compared to the subtraction and other source models. The boundary approach is studied for the subtraction and localized subtraction source model.

2 Background

In this chapter the relevant mathematical models and methods for understanding the localized subtraction source model and its numerical solution are given. First, the models for the EEG and MEG forward problem are derived. For discretization the finite element method is described. In this scope, the continuous Galerkin method is introduced and applied to the EEG and MEG forward problem. Finally the transfer matrix approach to speed up the computation time is presented.

2.1 Derivation of the Forward Problem

This section will follow [7] and [10] to derive the EEG and MEG forward problem.
The main equations used to describe how electric potentials and magnetic fields are generated by charges, currents and changes of the fields are the Maxwell equations. According to [7] it is sufficient to use their quasi-static approximation. We also assume that the permeability of the tissue in the head is that of the free space.

Let E be the electric field, ρ the electric charge density and ϵ_0 the permittivity of free space.
The quasi-static Maxwell equations related to the electrical part are

$$\nabla \times E = 0, \tag{1}$$

$$\nabla \cdot E = \frac{\rho}{\epsilon_0}. \tag{2}$$

Furthermore let B be the magnetic field (B-field), μ_0 the permeability of free space and j the total current density produced by neuronal activity.
The quasi-static Maxwell equations related to the magnetic part are

$$\nabla \times B = \mu_0 j, \tag{3}$$

$$\nabla \cdot B = 0. \tag{4}$$

In bio-electromagnetism the total current density is split into the the primary current j^p and the secondary current j^s:

$$j(r) = j^p(r) + j^s(r), \quad r \in \mathbb{R}^3. \tag{5}$$

The primary current is seen as the source of the electric acivity. Typically it is written as a mathematical point dipole,

$$j^p(r) = M \cdot \delta(r - r_0), \tag{6}$$

where $M \in \mathbb{R}^3$ is the dipole moment (strength and orientation of the dipole) and δ the Dirac delta distribution centered in the dipole position $r_0 \in \mathbb{R}^3$.
The secondary or return current is the result of the electric field and describes the passive current flow in the remaining head,

$$j^s(r) = \sigma(r)E(r), \tag{7}$$

where the tensor σ stands for the electric conductivity of the conducting medium.

2.1.1 The EEG Forward Problem

For the electrical forward problem we consider (1) and (3) of the Maxwell equations.
Because the curl of a gradient is always zero, we can conclude from (1), that there exists a potential u such that

$$E = - \nabla u.$$

Therefore the secondary current (7) can be rewritten as

$$j^s = -\sigma \nabla u. \tag{8}$$

Taking the divergence of (3), we get $\nabla \cdot (\nabla \times B) = 0$ for the left-hand side. Using (5) and (8) then leads to

$$\begin{array}{rrcl} & 0 & = & \nabla \cdot (\mu_0 j) \\ \Leftrightarrow & 0 & = & \nabla \cdot (j^p + j^s) \\ \Leftrightarrow & -\nabla \cdot j^s & = & \nabla \cdot j^p \\ \Leftrightarrow & \nabla \cdot (\sigma \nabla u) & = & \nabla \cdot j^p. \end{array}$$

The last equation is the inhomogeneous Poisson equation for the EEG forward problem in the head domain.
As the flux $\sigma \nabla u$ is supposed to be continous in Ω while the conductivity σ is zero outside of the head domain, we have a homogeneous Neumann boundary condition on the head surface:

$$\langle \sigma \nabla u, n \rangle = 0.$$

In summary we obtain the so-called *strong formulation* of the EEG forward problem.

Definition 1 (Strong formulation of the EEG forward problem) *Let $\Omega \subset \mathbb{R}^3$ be the head domain, σ the conductivity tensor, j^p the primary current produced by the neuronal activity and n the unit outer normal on $\partial\Omega$. The strong formulation of the EEG forward problem is to find $u \in C^2(\Omega) \cap C^0(\partial\Omega)$ such that*

$$\begin{cases} \nabla \cdot (\sigma \nabla u) = \nabla \cdot j^p & \text{in } \Omega \\ \langle \sigma \nabla u, n \rangle = 0 & \text{on } \partial\Omega. \end{cases}$$

We can only ensure a unique solution of the strong formulation if we apply certain restrictions.
Firstly, the conductivity tensor σ needs to be continuous. In our framework, it is only assumed to be piecewise constant, with incontinuities across the surfaces of the different tissues (e.g gray matter, cerebrospinal fluid, skull, skin). In section 2.2 this issue will be approached by introducing a *finite element discretization* based on the *weak formulation* of the problem.
Secondly, the term $f := \nabla \cdot j^p$, that we will from now on refer to as the *source term*, needs to be a regular function. But as the primary current j^p is usually represented as a point dipole (6), the source term is singular in the dipole position. There are several ways to handle the singularity of the source term. We generally call these strategies *source models* and will take a closer look at the *subtraction* source model in section 3.

2.1.2 The MEG Forward Problem

In this section we derive Biot-Savart's law to calculate the magnetic B-field following [10].
Regarding the magnetic measurements, we want to know the magnetic flux Φ, generated by the neuronal activity. It can be computed as the integral of the B-field over the sensor surface S:

$$\Phi = \int_S B \cdot ds.$$

Concerning the B-field we know that $\nabla \cdot B = 0$ (4), and as the divergence of a curl is always zero, we can introduce a magnetic vector potential A such that

$$B = \nabla \times A. \tag{9}$$

The potential A is uniquely defined by (9) and the choice of the Coloumb gauge, i.e. $\nabla \cdot A = 0$.
Reshaping the Maxwell equation (3) by using (9) and the Coloumb gauge leads to the Poisson equation

$$\begin{aligned}\mu_0 j &= \nabla \times B \\ &= \nabla \times (\nabla \times A) \\ &= \nabla(\nabla \cdot A) - \triangle A \\ &= - \triangle A.\end{aligned}$$

which solution is given by

$$A(r) = \frac{\mu_0}{4\pi} \int_\Omega \frac{j(r')}{|r - r'|} d^3 dr'.$$

This leads to

$$\begin{aligned}B(r) &= \nabla \times A(r) \\ &= \frac{\mu_0}{4\pi} \int_\Omega \nabla \times \left(\frac{j(r')}{|r - r'|} \right) d^3 r'.\end{aligned}$$

Note, that r is a point outside of Ω as the sensors that measure the B-field are outside of the head domain. We apply the product rule to the content of the integral. Because the nabla operator acts depending on the variable r, the curl of $j(r')$ disappears:

$$\begin{aligned}\nabla \times \left(\frac{j(r')}{|r - r'|} \right) &= \nabla \left(\frac{1}{|r - r'|} \right) \times j(r') + \frac{1}{|r - r'|} \nabla \times j(r') \\ &= -\frac{r - r'}{|r - r'|^3} \times j(r') \\ &= j(r') \times \frac{r - r'}{|r - r'|^3}\end{aligned}$$

As for the B-field, we then receive

$$B(r) = \frac{\mu_0}{4\pi} \int_\Omega j(r') \times \left(\frac{r - r'}{|r - r'|^3} \right) d^3 dr',$$

which is known as Biot-Savart's law. Now we plug in the information we have about the source j, that is (5), (6) and (8), to obtain

$$\begin{aligned}B(r) &\overset{(5)}{=} \frac{\mu_0}{4\pi} \int_\Omega (j^p(r') + j^s(r')) \times \left(\frac{r - r'}{|r - r'|^3} \right) d^3 dr' \\ &= \frac{\mu_0}{4\pi} \int_\Omega j^p(r') \times \left(\frac{r - r'}{|r - r'|^3} \right) d^3 dr' + \frac{\mu_0}{4\pi} \int_\Omega j^s(r') \times \left(\frac{r - r'}{|r - r'|^3} \right) d^3 dr' \\ &\overset{(6),(8)}{=} \frac{\mu_0}{4\pi} M \times \frac{r - r_0}{|r - r_0|^3} - \frac{\mu_0}{4\pi} \int_\Omega \sigma \nabla u(r') \times \frac{r - r'}{|r - r'|^3} d^3 r'.\end{aligned}$$

We observe that the B-field consists of two contributions,

$$B(r) = B^p(r) + B^s(r), \tag{10}$$

where the primary B-field

$$B^p(r) := \frac{\mu_0}{4\pi} M \times \frac{r - r_0}{|r - r_0|^3} \tag{11}$$

emerges from the primary current at the dipole position r_0 and the secondary B-field

$$B^s(r) := -\frac{\mu_0}{4\pi} \int_\Omega \sigma \bigtriangledown u(r') \times \frac{r - r'}{|r - r'|^3} d^3r' \tag{12}$$

emerges from the secondary current.
The primary B-field B^p can be calculated analytically. The secondary B-field B^s depends on the solution u of the EEG forward problem and therefore has to be computed numerically if u is a numerical solution.

2.2 The Finite Element Method

In this section we introduce the finite element method (FEM) to solve the EEG and MEG forward problem.
As the conductivity tensor σ is only piecewise constant in each of the different brain tissues, we can not find a sufficiently smooth solution of the strong formulation seen in definition 1. We can, however, prove the existence of a unique *weak solution* in the context of a *weak formulation*. The weak solution is not differentiable in the classical sense, but still solves the partial differential equation in terms of weak derivatives.
Furthermore, the weak formulation reduces the partial differential equation to a linear system, which solution is approximated on the *finite element space*. There are several ways to choose the finite element space. In this thesis we present two of them, which lead to a *continuous* and *discontinuous Galerkin finite element approach*.

2.2.1 A Weak Formulation

Generally a weak formulation is of the form:

$$\text{Find } u \in V \text{ such that } a(u, v) = l(v) \quad \forall v \in V, \tag{13}$$

where a is a bilinear form and l a linear functional on V. The space V is called a test function space containing the test functions $v \in V$. The specifics of a, l and V can wary for different approaches.
We want to follow [13] to derive a weak formulation that has a unique solution and is consistent with the strong formulation, meaning that every solution of the strong formulation is also a solution of the weak formulation.
In [2] it is shown that (13) is equivalent to the variational problem

$$u = \arg\min_{v \in V} J(v), \qquad J(v) := \frac{1}{2} a(u, v) - l(v),$$

if a is a symmetric and positive-definite.
Under these conditions we can use the theorem of Lax-Milgram to proof existance and uniqueness of the weak solution.

Theorem 1 (Lax-Milgram) *Let $(H, \langle \cdot, \cdot \rangle)$ be a Hilbert space, $a(\cdot, \cdot)$ an elliptic bilinear form (i.e. a is symmetric, positive-definite and $a(v, v) > \alpha \|v\|_H^2 \ \forall v \in H, \alpha > 0$) and $l \in H'$ a continuous linear functional. Then there exists a unique solution $u \in H$ of the variational problem*

$$u = arg\ min_{v \in H} J(v), \qquad J(v) := \frac{1}{2} a(u, v) - l(v),$$

Proof. [2]

As the base of our Hilbert space we choose $V \subset L^2(\Omega)$ with the scalar product

$$\langle u, v \rangle_{L^2} := \int_\Omega u(x)v(x)dx.$$

Then we multiply the Poisson equation of the strong formulation with a test function and integrate over Ω, leading to

$$\int_\Omega \nabla \cdot (\sigma \nabla u)v \, dx = \int_\Omega fv \, dx.$$

Applying Gauss' theorem to the left-hand side and considering the Neumann boundary condition gives

$$\int_\Omega \nabla \cdot (\sigma \nabla u)v \, dx \overset{\text{Gauss}}{=} -\int_\Omega \langle \sigma \nabla u, \nabla v \rangle \, dx + \int_{\partial\Omega} \underbrace{\langle \sigma \nabla u, n \rangle}_{=0} v \, ds = -\int_\Omega < \sigma \nabla u, \nabla v > \, dx.$$

Now we define the (bi)linear forms

$$\begin{array}{lll} a(u,v) & := -\langle \sigma u, v \rangle_{L^2} & = -\int_\Omega \langle \sigma \nabla u, \nabla v \rangle \, dx, \\ l(v) & := \langle f, v \rangle_{L^2} & = \int_\Omega fv \, dx. \end{array}$$

In [2] it is proven that this choice of a and l leads to consistency with the strong formulation.

The conditions to use the theorem of Lax-Milgram, namely that a needs to be elliptic on V, direct the specific choice of the test function space. Following [13] the appropriate space is the Sobolov space $H^1(\Omega)$ of weakly differentiable functions which needs to be further restricted to $H^1_*(\Omega) := \left\{ f \in H^1(\Omega) \mid \int_\Omega f dx = 0 \right\}$ because of the Neumann boundary condition. In conclusion we define the following weak formulation that has a unique solution.

Definition 2 (Weak formulation of the EEG forward problem)
Let $V := H^1_*(\Omega) = \left\{ f \in H^1(\Omega) \mid \int_\Omega f dx = 0 \right\}$ be the space of weakly differentiable functions with zero mean. The weak formulation of the EEG forward problem is to find $u \in V$ such that $a(u,v) = l(v) \; \forall v \in V$, where

$$\begin{aligned} a(u,v) &:= -\int_\Omega \langle \sigma \nabla u, \nabla v \rangle \, dx, \\ l(v) &:= \int_\Omega fv \, dx. \end{aligned}$$

It must be remarked that this formulation demands that $f \in L^2(\Omega)$, which is not the case when choosing the mathematical point dipole as the primary current. As already mentioned, this is a problem that will be handled by source models. We will see that the right-hand side $l(v)$ changes with the choice of the source model, while the left-hand side $a(u,v)$ stays the same.

2.2.2 Finite Element Spaces: The CG- and DG-FEM

The weak formulation from the previous section was defined on the infinte-dimensional test function space $V = H^1_*$. In order to reduce the linear system to a finite amount of equations we make an approximation on the *finite element space* V_h. There are serveral possible choices for V_h. Two of them are presented in this section, that lead to the *continuous* and *discontinuous Galerkin* finite element method. This section follows [13] where more details can be found.
Generally, we imagine a subdivision of the head domain Ω into a finite number of subsets, e.g. in shape of tetrahedrons or hexahedrons. The subsets should form a *triangulation*.

Definition 3 (Triangulation) *A triangulation of a domain Ω is a set $T_h(\Omega) = \{E_0, E_1, ..., E_{m-1}\}$ of open convex polytopes $E_i \subset \Omega$ such that*

- $\overline{\Omega} = \bigcup_{E \in T_h} \overline{E}$,
- $E_i \cap E_j = \emptyset, i \neq j$,
- *Each $E \in T_h$ is closed and its interior $\mathring{E}$ is non-empty*
- *For each $E \in T_h$ the boundary ∂E is Lipschitz-continous*

The subsets E_0,E_1,...,E_{m-1} are called finite elements.

Based on the triangulation we define a finite-dimensional function space V_h that satisfies the following conditions:

1. The functions $v_h \in V$ are piecewise polynomial (on the finite elements).
2. The basis functions of V_h have small support.

If we replace V with V_h in the weak formulation (13), it becomes:

$$\text{Find } u_h \in V_h \text{ such that } a(u_h, v_h) = l(v_h) \quad \forall v \in V.$$

Later in this thesis, we will often see this expression when we define the finite element discretizations. In terms of numerical implementation we want to use the basis functions to derive an equivalent matrix-vector representation. As V_h is finite-dimensional we can find a finite basis $\{\varphi_1, ..., \varphi_{N_h}\}$. Therefore, each $v_h \in V_h$ can be represented by

$$v_h(x) = \sum_{i=1}^{N_h} v_i \varphi_i(x) \tag{14}$$

for suitable $v_i \in \mathbb{R}$. When we plug (14) into the weak formulation and use that a is bilinear and l is linear, we see that it is equivalent to

$$\text{Find } u_h \in V_h \text{ such that } a(u_h, \varphi_i) = l(\varphi_i) \quad \forall i = 1, .., N_h.$$

The discrete solution u_h also has a representation in terms of the basis, i.e. $u_h(x) = \sum_{i=1}^{N_h} u_i \varphi_i(x)$. The coefficients u_i are unknown, but as u_h is by definition also a member of the finite element space, they need to exist if u_h exists. Therefore the weak formulation is equivalent to

$$\text{Find } u_j \in \mathbb{R} \text{ such that } \sum_{j=1}^{N_h} u_j a(\varphi_j, \varphi_i) = l(\varphi_i) \quad \forall i = 1, .., N_h,$$

The bilinear and linear forms can be written as a matrix $A = (a_{i,j})_{i,j=1,...,N_h}$ (known as the *stiffness matrix*) and a vector $l = (l_i)_{i=1,...,N_h}$, where

$$a_{i,j} = a_h(\varphi_i, \varphi_j)$$
$$l_i = l_h(\varphi_i)$$

Finally the discrete weak formulation can be written as a linear system of N_h equations,

$$A\mathbf{u} = l, \tag{15}$$

with the unknown vector $\mathbf{u} = (u_i)_{i=1,..,N_h}$.
In the following we will have a closer look at two precise examples of the finite element space.

The CG- and DG-FEM

In the *continuous Galerkin* finite element method (CG-FEM) the finite element space is chosen as

$$V_h = X_h^r := \{v_h \in C^0 : v_h|_E \in P_r, \ \ \forall E \in T_h\},$$

where P_r is the space of polynomial functions of degree $r \in \mathbb{N}$. This means that the test functions $v_h \in X_h^r$ are piecewiese polynomial on the finite elements and globally continuous. As the finite element space $V_h = X_h^r$ is a subset of the Sobolov space $V = H^1(\Omega)$, the CG-FEM is called a conforming FEM.
Another option for choosing the finite element space leads to the *discontinuous Galerkin* finite element method (DG-FEM). Here we have

$$V_h = Y_h^r := \{v \in L^2(\Omega) : v|_E \in P_r(E), \ \ \forall E \in T_h\}.$$

Again P_r is a vector space containing polynomial functions of degree $r \in \mathbb{N}$. In the DG-FEM the test functions $v_h \in Y_h^r$ are piecewise polynomial and in particular continuous on each of the finite elements, but, in comparison to the CG-FEM, not restricted to be globally continous.
We will see that the set-up and implementation of the DG-FEM are more complicated and costly than the CG-FEM. However, it sometimes offers higher accuracy. There are, for example, cases of "skull leakage effects" in areas where the diameter of the finite elements is close to the thickness of the skull (particulary in small/children's brains). The DG-FEM can reduce these effects. Furthermore the DG-FEM guarantees the conservation of charge property in the discrete formulation. See [6] for a more precise comparison of the two approaches.

The choice of the polynomial space P_r depends on the geometry of the finite elements. If the polytopes are tetrahedra we define

$$P_r = \mathbb{P}_r := span\left\{x^\alpha \mid \alpha \in \mathbb{N}^3, \|\alpha\|_1 \leq r\right\},$$

using the multi-index notation $x^\alpha = \prod_i x_i^{\alpha_i}$.

If the triangulation is made of hexahedra we instead define

$$P_r = \mathbb{Q}_r := span\left\{x^\alpha \mid \alpha \in \mathbb{N}^3, \|\alpha\|_\infty \leq r\right\}.$$

In this thesis we will use piecewiese linear test functions, i.e. $r = 1$. For this case we now take a closer look at the basis functions and basis representation of a function in V_h (cf. 14). When we want to write a function $v_h \in V_h$ as a linear combination of the basis functions, $v_h(x) = \sum_{i=1}^{N_h} v_i \varphi_i(x)$, we need to find the correct values v_i. In the linear case, each v_h is uniquely defined by its values at the vertices of each finite element. Therefore we can choose

$$\varphi_j(N_i) := \delta_{i,j}, \quad j = 1, ..., N_h$$

as the basis functions, where $N_1, ..., N_{N_h}$ are the vertices of the finite elements and thus $v_i := v_h(N_i)$, $i = 1, ..., N_h$. The solution vector $\mathbf{u} = (u_i)_{i=1,..,N_h}$ can be interpreted as potential evaluated at the elements' vertices.
The set of vertices are called the nodes of the triangulation. For the CG-FEM, if two or more elements have vertices that share the same node, a test function must have the same value on each of those vertices (to obtain global continuity). Therefore $N_1, ..., N_{N_h}$ are actually the nodes of the triangulation. The natural number N_h corresponds to the dimension of V_h and ultimately the size of the linear system.

So, for the CG-FEM N_h = #(nodes of the triangulation) and for the DG-FEM N_h = #(vertices per element) · #elements. In case of hexahedra the amount of vertices per element is eight, whereas in case of tetrahedra it is four. Note that the size of the resulting DG-FEM system is much bigger than in the CG-FEM case, which leads to a longer computation time.

2.2.3 Solving the EEG Forward Problem

In this section, we define the CG- and DG-FEM for the EEG forward problem. As seen in section 2.2.1 we multiply the Poisson equation from definition 1 with a test function (the choice of the test function space was explained in section 2.2.2) and integrate over Ω. We then use Gauss' theorem and the Neumann boundary condition to manipulate the left-hand side.
For the CG-FEM this simply leads to the following formulation:

Definition 4 (The CG-FEM for the EEG Forward Problem) *The CG-FEM for the EEG forward problem is to find $u_h \in X_h^1$ such that $a(u_h, v_h) = l(v_h)\ \forall v_h \in X_h^1$, where*

$$a(u_h, v_h) := -\int_\Omega \langle \sigma \bigtriangledown u_h, \bigtriangledown v_h \rangle \, dx,$$
$$l(v_h) := \int_\Omega f v_h \, dx.$$

In the DG-FEM framework we generally want to use the same strategy to derive the weak formulation. However, when using Gauss' theorem, we must consider the discontinuities on the intersections between elements. Thus we can not apply Gauss to the integral over the whole domain Ω. Instead we first treat a single element $E \in T(\Omega)$ and later sum over all elements. During this procedure we obtain integrals over the finite elements' boundaries, which are also the intersections between elements or an element and the boundary of the domain. The set of these intersections is called the *skeleton* of the triangulation.

Definition 5 (Skeleton) *The internal skeleton of a triangulation $T_h(\Omega)$ is defined as*

$$\Gamma_h^{int} := \{\underbrace{\partial E_i \cap \partial E_j}_{\gamma_{ij}} \mid \ E_i, E_j \in T_h(\Omega), E_i \neq E_j, |\gamma_{ij}| > 0\}$$

and the skeleton is defined as

$$\Gamma_h := \Gamma_h^{int} \cup \{\underbrace{\partial E_i \cap \partial \Omega}_{\gamma_i} | E_i \in T_h(\Omega), |\gamma_i| > 0\},$$

On the skeleton, the functions in Y_h^r are not uniquely defined but might have two different values corresponding to the two neighbouring elements. The *jump* describes the difference between those values.

Definition 6 (Jump) *The jump of a scalar funciton u or a vector-valued funcion v on an intersection γ_{ij} between two elements $E_i, E_j \in T_h(\Omega)$ is defined as*

$$[\![u]\!] := u|_{E_i} n_{E_i} + u|_{E_j} n_{E_j},$$
$$[\![v]\!] := \langle v|_{E_i}, n_{E_i} \rangle + \left\langle v, |_{E_j} n_{E_j} \right\rangle,$$

where n_{E_i} and n_{E_j} denote the unit outer normal vectors on E_i and E_j. The normal vectors are opposing, i.e. $n_i = -n_j$.
The jump of a scalar funtion is a vector and the jump of a vector-valued function is a scalar.

Another operator that appears in the DG-FEM formulation is the *weighted average*:

Definition 7 (Weighted average) *The weighted average of a (scalar or vector-valued) function u on an intersection γ_{ij} between two elements $E_i, E_j \in T_h(\Omega)$ is defined as*

$$\{u\} := \omega_i u|_{E_i} + \omega_j u|_{E_j}$$

with two weights $\omega_i, \omega_j \in \mathbb{R}$ where $\omega_i + \omega_j = 1$. We define these weights as

$$\omega_i := \frac{\delta_j}{\delta_i + \delta_j} \qquad \omega_j := \frac{\delta_i}{\delta_i + \delta_j}$$
$$\delta_i := n_i^t \sigma n_i \qquad \delta_j := n_j^t \sigma n_j$$

where n_{E_i} and n_{E_j} denote the unit outer normal vectors on E_i and E_j.
The skew-weighted average is defined as

$$\{u\}^* := \omega_j u|_{E_i} + \omega_i u|_{E_j}$$

The derivation of a DG-FEM formulation is not as simple as in the CG-FEM framework. As this is not the focus of this thesis, we will not go into detail, but only briefly introduce the *symmetric weighted interior penalty* DG-FEM[1] that was derived in [4].

Definition 8 (The DG-FEM for the EEG forward problem) *The symmetric weighted interior penalty DG-FEM (SWIPG) for the EEG forward problem is to find $u_h \in Y_h^1$ such that $a(u_h, v_h) + J(u_h, v_h) = l(v_h)\ \forall v_h \in Y_h^1$, where*

$$a(u_h, v_h) := -\int_\Omega \langle \sigma \bigtriangledown u_h, \bigtriangledown v_h \rangle \, dx + \int_{\Gamma_h^{int}} \langle \{\sigma \bigtriangledown u_h\}, [\![v_h]\!] \rangle + \langle \{\sigma \bigtriangledown v_h\}, [\![u_h]\!] \rangle \, ds,$$
$$J(u_h, v_h) := -\eta \int_{\Gamma_h^{int}} \frac{\hat{\sigma}_\gamma}{\hat{\boldsymbol{h}}_\gamma} \langle [\![u_h]\!], [\![v_h]\!] \rangle,$$
$$l(v_h) := \int_\Omega f v_h \, dx.$$

The weighting parameter $\hat{\sigma}_\gamma$ on an intersection γ between two elements E_i and E_j is the harmonic average of the projected conductivity tensors (cf. definition 7)

$$\hat{\sigma}_\gamma := \frac{2\delta_i \delta_j}{\delta_i + \delta_j}.$$

The parameter $\hat{\boldsymbol{h}}_\gamma$ depends on the local mesh size and is defined as (REF)

$$\hat{\boldsymbol{h}}_\gamma := \frac{min(|E_i|, |E_j|)}{|\gamma|}$$

In comparison to the CG-FEM the term $a(u_h, v_h)$ consists of an additional intergral over the interior skeleton. This integral results from applying Gauss' theorem to individual elements. Whereas the integral over the domain's boundary vanishes because of the Neumann boundary condition, the sum of the integrals over the interior skeleton lead to the first half of the skeleton integral, $\int_{\Gamma_h^{int}} \langle \{\sigma \bigtriangledown u_h\}, [\![v_h]\!] \rangle \, ds$. The second half, the symmetry term $\int_{\Gamma_h^{int}} \langle \{\sigma \bigtriangledown v_h\}, [\![u_h]\!] \rangle \, ds$, was added to make the bilinear form symmetric with regard to Lax-Milgram (theorem 1).
Furthermore we have an additional penalty term $J(u_h, v_h)$ that is used to obtain coercivity of the left-hand side while penalizing jumps in the potential on the internal skeleton.

2.2.4 Solving the MEG Forward Problem

As mentioned in section 2.1.2 the secondary B-field has to be computed numerically if we have a numerical solution u_h of the EEG forward problem. In the FEM framework u_h is a member of the finite element space V_h and is represented as $u_h(r) = \sum_{j=1}^{N_h} u_j \varphi_j(r), \forall r \in \Omega$, where $\{\varphi_j\}_j$ is a basis of V_h (cf. (14)). Plugging this into (12) leads to the following discretization of the secondary B-field, evaluated at c_n, the center of the $n-th$ coil:

[1] The SWIPG is not the only possibility for a discontinuous Galerkin method. For a more general description of the method, as well as a mathematical analysis of its properties see [1].

$$B_h^s(c_n) = \sum_{j=1}^{N_h} u_j(-\frac{\mu_0}{4\pi}) \int_\Omega \sigma \bigtriangledown \varphi_j(r') \times \frac{c_n - r'}{|c_n - r'|^3} d^3r,' \quad n = 1, ..., s_{meg}, \tag{16}$$

where s_{meg} is the center of the n-th coil. This equation can be written in matrix form,

$$B_h^s = S\mathbf{u},$$

where $\mathbf{u} = (u_i)_{i=1,...,N_h}$ and the so-called *secondary magnetic field integration matrix* $S = (S_{n,j})_{n,j} \in \mathbb{R}^{s_{meg} \times N_h}$ is given by

$$S_{n,j} = (-\frac{\mu_0}{4\pi}) \int_\Omega \sigma \bigtriangledown \varphi_j(r') \times \frac{c_n - r'}{|c_n - r'|^3} d^3r'. \tag{17}$$

2.3 The Transfer Matrix Approach

The discretization of the EEG forward problem results in a linear system $A\mathbf{u} = l$ (cf. (15)) that has to be solved for $\mathbf{u}$.
A fast way to solve for $\mathbf{u}$ is the transfer matrix approach, that makes use of the fact that we are only interested in the entries of $\mathbf{u}$ that correspond with a sensor location. This approach can also calculate the secondary magnetic field B_h^s without having to solve for $\mathbf{u}$ first. The description of the transfer matrix apporach follows [14].
Even though calculating the inverse of A is too costly numerically, we could, theoretically, write

$$\mathbf{u} = A^{-1}l. \tag{18}$$

For most applications it is sufficient to know $\mathbf{u} \in \mathbb{R}^{N_h}$ at the EEG sensor locations, therefore we multiply it with a restriction matrix R that maps $\mathbf{u}$ to the non-reference electrodes. We define the projected potential as $u_{eeg} := R\mathbf{u}$. The matrix $R \in \mathbb{R}^{(s_{eeg}-1)\times N_h}$, where s_{eeg} is the number of EEG sensors, has only one non-zero entry with value 1 in each row. The column of the 1-value entry corresponds to the node of the sensor location.
Regarding the MEG forward problem we want to know the magnetic field at the MEG sensor locations, B_h^s, which is obtained by multiplying $\mathbf{u}$ with the secondary magnetic field integration matrix S (cf. (17)).
In summary we have:

$$u_{eeg} = R\mathbf{u} \overset{(18)}{=} R(A^{-1}l) = (RA^{-1})l = B_{EEG}l,$$
$$B_h^s = S\mathbf{u} \overset{(18)}{=} S(A^{-1}l) = (SA^{-1})l = B_{MEG}l.$$

The matrices $B_{EEG} := RA^{-1}$ and $B_{MEG} = SA^{-1}$ are the so called transfer matrices. To calculate them, instead of solving $A\mathbf{u} = l$ for $\mathbf{u}$, we solve the similar (adjoint) problems

$$A[B_{EEG}^T] = R^T$$
$$A[B_{MEG}^T] = S^T$$

for each row of R or S, respecitvely. We received these equations by multiplying the definitions of the transfer matrices with A from the right, transposing the equations and using the symmetry of A.
The computational effort of solving for the transfer matrices is actually higher than the effort of solving directly for $\mathbf{u}$, because $\mathbf{u}$ has only one column while B_{EEG}^T and B_{MEG}^T have as many columns as there are sensors. However, the advantage of the transfer matrix approach is the fact that the transfer matrices do not depend on the right-hand side l. They can be precomputed, stored and then multiplied with different

right-hand sides to obtain u_{eeg} and B_h^s. As in practice the number of right-hand sides ($> 10^4$) surpasses the number of sensors ($\approx 10^2$), the transfer matrix approach immensely reduces the computation time (see [14] for a detailed calcuation of the computational effort).
The total computation time for the transfer matrix approach can be divided into three steps: The computation of the transfer matrices, assembling a right-hand side vector l and a matrix-vector multiplication. The duration of the last two steps are proportional to the number of non-zero entries in l (when using sparse vector types). Therefore source models like the Partial Integration or Venant approach, that have a sparse right-hand side, outperform the subtraction source model (that has no non-zero entries) in regards to computation time. With the localized subtraction source model we will introduce a strategy to reduce the number of non-zero entries for the subtraction source model.

3 The Subraction Source Model

The mathematical dipole that we used to model the primary current j^p of the electric activity leads to a singularity in the source term $f = \nabla \cdot j^p$. The singularity prevents us from finding a unique solution of the strong as well as the weak formulations. Source models are strategies of treating this singularity. The subtraction source model is theoretically well understood, including proofs for existence and uniqueness of solutions and convergence analysis [5] [15].

Let $\Omega_\infty \subset \Omega$ be a non-empty open neigbourhood around the dipole position r_0. In Ω_∞ we assume a constant and isotropic conductivity, i.e. $\sigma|_{\Omega_\infty} = \sigma^\infty I_3$, $\sigma^\infty \in \mathbb{R}^3$. For the sake of simplicity we will denote both the scalar and $\sigma|_{\Omega_\infty}$ as σ^∞.
The overall conductivity σ is split into

$$\sigma = \sigma^\infty + \sigma^{corr}, \tag{19}$$

where σ^{corr} corrects the difference between σ^∞ and the 'true' conductivity σ. Therefore σ^{corr} is zero inside Ω_∞. Likewise the potential u is split into

$$u = u^\infty + u^{corr}. \tag{20}$$

We call u^∞ the singularity potenital and u^{corr} the correction potential.
The singularity potential u^∞ is defined as the solution of the Poisson equation in an unbounded and homogeneous volume conductor with constant and isotropic conductivity σ^∞:

$$\nabla \cdot (\sigma^\infty \nabla u^\infty) = \nabla \cdot j^p =: f \quad \text{in } \mathbb{R}^3. \tag{21}$$

Equation (21) is equivalent to $\triangle u^\infty = \frac{\nabla \cdot j^p}{\sigma^\infty}$ and in this simple case u^∞ can be calculated analytically and is given by [15]

$$u^\infty(r) = \frac{1}{4\pi\sigma^\infty} \frac{\langle M, (r - r_0)\rangle}{|r - r_0|^3}, \quad r \in \mathbb{R}^3, \tag{22}$$

where r_0 is the dipole position and M is the dipole moment (cf. (6)). The singularity potential is singular in r_0, but smooth everywhere else.

To find the correction potential u^{corr} we plug the splitting of the conductivity and potential into the original strong formulation of the forward problem (definition 1). The Poisson equation transforms to

$$\begin{aligned}\nabla \cdot (\sigma \nabla u) &= \nabla \cdot (\sigma \nabla u^{corr}) + \nabla \cdot (\sigma \nabla u^\infty) \\ &= \nabla \cdot (\sigma \nabla u^{corr}) + \nabla \cdot (\sigma^{corr} \nabla u^\infty) + \underbrace{\nabla \cdot (\sigma^\infty \nabla u^\infty)}_{\overset{(21)}{=} f} = f,\end{aligned}$$

and the boundary condition becomes

$$\langle \sigma \nabla u, n\rangle = \langle \sigma \nabla u^{corr}, n\rangle + \langle \sigma \nabla u^\infty, n\rangle = 0.$$

In summary we obtain the following strong formulation.

Definition 9 (Strong formulation using the subtraction source model) *The strong formulation using the subtraction source model is to find* $u^{corr} \in C^2(\Omega) \cap C^0(\partial\Omega)$ *such that*

$$\begin{cases} \nabla \cdot (\sigma \nabla u^{corr}) &= -\nabla \cdot (\sigma^{corr} \nabla u^{\infty}) & \text{in } \Omega \\ \langle \sigma \nabla u^{corr}, n \rangle &= -\langle \sigma \nabla u^{\infty}, n \rangle & \text{on } \partial\Omega. \end{cases}$$

The singular source term f vanished, because its contribution is already included in the singularity potential. The singularity potential in the new right-hand side in fact still has a singularity in the dipole position, but it is multiplied by the correction potential. As σ^{corr} is zero in the small domain Ω_∞ around the dipole position, the singularity vanishes.

After solving for the correcting potential, u^{∞} is added to obtain the full potential u. This step is called post processing.

3.1 Solving the EEG Forward Problem using the CG-FEM

To derive a CG-FEM formulation (cf. section 2.2) for the subtraction source model we multiply the Poisson equation from definition 9 with a test function $v_h \in X_h^1$, integrate over the head domain and apply Gauss' theorem to both sides. Now we are looking for $u_h^{corr} \in X_h^1$ that solves

$$-\int_\Omega \langle \sigma \nabla u_h^{corr}, \nabla v_h \rangle \, dx + \int_{\partial\Omega} \langle \sigma \nabla u_h^{corr}, n \rangle \, v_h \, ds = \int_\Omega \langle \sigma^{corr} \nabla u^{\infty}, \nabla v_h \rangle \, dx - \int_{\partial\Omega} \langle \sigma^{corr} \nabla u^{\infty}, n \rangle \, v_h \, ds$$

for all test functions. We can use the boundary condition from definition 9 to manipulate the boundary integral on the right-hand side. This leads to

$$-\int_\Omega \langle \sigma \nabla u_h^{corr}, \nabla v_h \rangle \, dx - \int_{\partial\Omega} \langle \sigma \nabla u^{\infty}, n \rangle \, v_h \, ds = \int_\Omega \langle \sigma^{corr} \nabla u^{\infty}, \nabla v_h \rangle \, dx - \int_{\partial\Omega} \langle \sigma^{corr} \nabla u^{\infty}, n \rangle \, v_h \, ds.$$

Now we can bring the boundary term to the right-hand side:

$$-\int_\Omega \langle \sigma \nabla u_h^{corr}, \nabla v_h \rangle \, dx = \int_\Omega \langle \sigma^{corr} \nabla u^{\infty}, \nabla v_h \rangle \, dx + \int_{\partial\Omega} \langle \sigma^{\infty} \nabla u^{\infty}, n \rangle \, v_h \, ds.$$

This equations can now be formulated in terms of a bilinear and linear form, as we have seen in section 2.2.

Definition 10 (The CG-FEM using the Subtraction Source Model) *The CG-FEM using the subtraction source model is to find* $u_h^{corr} \in X_h^1$ *such that* $a(u_h^{corr}, v_h) = l(v_h) \; \forall v_h \in X_h^1$, *where*

$$\begin{aligned} a(u_h^{corr}, v_h) &:= -\int_\Omega \langle \sigma \nabla u_h^{corr}, \nabla v_h \rangle \, dx, \\ l(v_h) &:= \int_\Omega \langle \sigma^{corr} \nabla u^{\infty}, \nabla v_h \rangle \, dx + \int_{\partial\Omega} \langle \sigma^{\infty} \nabla u^{\infty}, n \rangle \, v_h \, ds. \end{aligned}$$

The bilinear form a is the same as in definition 2. In section 2.2.1 we have seen that this formulation has a unique solution if $l \in H_*^1(\Omega)$ (theorem 1). As σ^{corr} is zero in the domain Ω_∞ around the dipole position, where u^{∞} is singular (everywhere else it is smooth), the right-hand side l is bounded on $H^1(\Omega)$ and in particular the condition $l \in H_*^1(\Omega)$ is fulfilled [15]. Conclusively The CG-FEM subtraction approach has a unique solution.
The convergence analysis in [15] has found that sources close to a conductivity jump could have larger numerical erros (because of a strongly increasing convergence constant), which has been confirmed by numerical experiments.

3.2 A Boundary Approach for Solving the MEG Forward Problem

Let us revise (10), (11) and (12) from section 2.1.2, which are

$$B(r) = B^p(r) + B^s(r),$$

with the primary and secondary B-fields

$$B^p(r) := \frac{\mu_0}{4\pi} M \times \frac{r - r_0}{|r - r_0|^3},$$
$$B^s(r) := -\frac{\mu_0}{4\pi} \int_\Omega \sigma \bigtriangledown u(r') \times \frac{r - r'}{|r - r'|^3} d^3r'.$$

The primary B-field is an analytical expression while the secondary B-field depends on the electric potential u, the solution of the EEG forward problem.
Technically calculating the B-field is independent of the choice of the source model. When we have a discrete solution, for example resulting from a CG-FEM approach, we have derived a formulation of the secondary B-field (16) accordingly, that was

$$B_h^s(c_n) = \sum_{j=1}^{N_h} u_j (-\frac{\mu_0}{4\pi}) \int_\Omega \sigma \bigtriangledown \varphi_j(r') \times \frac{c_n - r'}{|c_n - r'|^3} d^3r'.$$

In the subtraction source model, the discrete solution $\mathbf{u} = (u_i)_{i=1,\dots,N_h}$ is obtained by calculating u^{corr} via the CG-FEM and then adding the analytical expression for u^∞ evaluated at the nodes of the triangulation. If we use (16) to calculate B_h^s we assume that $\mathbf{u}$ is a member of the finite element space X_h^1, specifically a piecewise linear function, but originally only u^{corr} was meant to be described as such. The singularity potential u^∞ is a singular function, so making a linear approximation, especially in the element where the dipole is located, leads to additional approxmation errors. To avoid these errors we can use the following approach presented by M. C. Piastra [10]. First, we split the secondary B-field via (20) into

$$B^s(r) = B^s_{corr}(r) + B^s_\infty,$$

where

$$B^s_{corr}(r) = -\frac{\mu_0}{4\pi} \int_\Omega \sigma \bigtriangledown u^{corr}(r') \times \frac{r - r'}{|r - r'|^3} d^3r',$$
$$B^s_\infty = -\frac{\mu_0}{4\pi} \int_\Omega \sigma \bigtriangledown u^\infty(r') \times \frac{r - r'}{|r - r'|^3} d^3r'.$$

Then the contribution of the correction potential, B^s_{corr}, can be calculated using (16) as usual. However, we need an alternative formula for the contribution of the singularity potential, B^s_∞. In [10] M.C. Piastra introduced a way to calculate B^s_∞ by substituting the volume integral by a boundary integral, as stated in the following proposition.

Proposition 1 *If $\sigma = \sigma^\infty I_3$, $\sigma^\infty \in \mathbb{R}$, is constant and isotropic it holds that*

$$\frac{\mu_0}{4\pi} \int_\Omega \sigma \bigtriangledown u^\infty \times \frac{r - r'}{|r - r'|^3} dx = \frac{\mu_0 \sigma^\infty}{4\pi} \int_{\partial\Omega} u^\infty \left(n \times \frac{r - r'}{|r - r'|^3} \right) ds, \tag{23}$$

Before we prove proposition 1, we observe the following lemmas.

Lemma 1 *If ϕ is a scalar function and F is a vector field, it holds true that*

$$\bigtriangledown \times (\phi F) = \bigtriangledown \phi \times F + \phi \bigtriangledown \times F,$$

Proof. See Appendix 1.

Lemma 2 *For a vector field F it holds true that*

$$\int_\Omega \nabla \times F \, dx = \int_{\partial\Omega} n \times F \, ds.$$

If ϕ is a scalar field, it then follows that

$$\int_\Omega \nabla \times (\phi F) \, dx = \int_{\partial\Omega} n \times (\phi F) \, ds = \int_{\partial\Omega} \phi (n \times F) \, ds.$$

Proof. See Appendix 2.

Now we can prove proposition 1.

Proof of Proposition 1.
At first we use that $\sigma = \sigma^\infty I_3$ is constant and isotropic. Therefore we can write

$$\frac{\mu_0}{4\pi} \int_\Omega \sigma \nabla u^\infty \times \frac{r - r'}{|r - r'|^3} dx = \frac{\mu_0 \sigma^\infty}{4\pi} \int_\Omega \nabla u^\infty \times \frac{r - r'}{|r - r'|^3} dx$$

We apply lemma 1 with $F(r) := \frac{r-r'}{|r-r'|^3}$ and $\phi(r) := u^\infty$ and obtain

$$\begin{aligned}\frac{\mu_0 \sigma^\infty}{4\pi} \int_\Omega \nabla u^\infty \times \frac{r - r'}{|r - r'|^3} dx &= \frac{\mu_0 \sigma^\infty}{4\pi} \int_\Omega \nabla \times \left(u^\infty \frac{r - r'}{|r - r'|^3} \right) dx - \frac{\mu_0 \sigma^\infty}{4\pi} \int_\Omega u^\infty \nabla \times \frac{r - r'}{|r - r'|^3} dx \\ &= \frac{\mu_0 \sigma^\infty}{4\pi} \int_\Omega \nabla \times \left(u^\infty \frac{r - r'}{|r - r'|^3} \right) dx\end{aligned}$$

The second integral vanished, because the vector field $F(r) = \frac{r-r'}{|r-r'|^3}$ is curl free (consider $f := r - r'$, then $\nabla \times F = \nabla \times (\nabla f) = 0$).

Now we apply lemma 2 to ϕF and get

$$\frac{\mu_0 \sigma^\infty}{4\pi} \int_\Omega \nabla \times \left(u^\infty \frac{r - r'}{|r - r'|^3} \right) dx = \frac{\mu_0 \sigma^\infty}{4\pi} \int_{\partial\Omega} u^\infty \left(n \times \frac{r - r'}{|r - r'|^3} \right) ds.$$

□

The condition that σ is constant and isotropic is not fulfilled on the whole domain Ω but at least in the small domain Ω_∞ around the dipole position, where the singularity potential is singular and the approximation errors would accure. Therefore we can use proposition 1 to write

$$\begin{aligned}B^s_\infty(r) &= -\frac{\mu_0}{4\pi} \int_{\Omega \setminus \Omega_\infty} \sigma \nabla u^\infty(r') \times \frac{r - r'}{|r - r'|^3} d^3 r' \\ &\quad - \frac{\mu_0}{4\pi} \int_{\Omega_\infty} \sigma \nabla u^\infty(r') \times \frac{r - r'}{|r - r'|^3} d^3 r' \\ &= -\frac{\mu_0}{4\pi} \int_{\Omega \setminus \Omega_\infty} \sigma \nabla u^\infty(r') \times \frac{r - r'}{|r - r'|^3} d^3 r' \\ &\quad - \frac{\mu_0 \sigma^\infty}{4\pi} \int_{\partial\Omega_\infty} u^\infty \left(n \times \frac{r - r'}{|r - r'|^3} \right) ds.\end{aligned}$$

To summarize, we define the boundary approach for calculating the secondary B-field:

Definition 11 (The boundary approach using the subtraction source model) *The boundary approach for calculating the secondary B-field B^s using the subtraction source model is*

$$B^s(r) = B^s_{corr}(r) + B^s_{\infty},$$

where

$$B^s_{corr}(r) = -\frac{\mu_0}{4\pi}\int_{\Omega} \sigma \bigtriangledown u^{corr}(r') \times \frac{r-r'}{|r-r'|^3} d^3r',$$

and

$$\begin{aligned} B^s_{\infty}(r) = &-\frac{\mu_0}{4\pi}\int_{\Omega\setminus\Omega_{\infty}} \sigma \bigtriangledown u^{\infty}(r') \times \frac{r-r'}{|r-r'|^3} d^3r' \\ &-\frac{\mu_0\sigma^{\infty}}{4\pi}\int_{\partial\Omega_{\infty}} u^{\infty}\left(n \times \frac{r-r'}{|r-r'|^3}\right) ds. \end{aligned}$$

4 The Localized Subtraction Source Model

Looking at the right-hand side of the discretized subtraction approach, we see that it consists of integrals including the singularity potential u^∞ (cf. definition 10). As the support of the singularity potential is the whole domain Ω, the resulting right-hand side vector l (cf. (15)) contains only non-zero entries. In regards to the transfer matrix approach, we would like to reduce the number of non-zero entries in l to speed up the computations. For this purpose, A. Nüßing introduced the localized subtraction source model [8].

The idea of the localized subtraction approach is to "cut off" the singularity potential outside of a domain $\Omega^\infty \subset \Omega$ around the source location:

$$u = \chi_{\Omega^\infty} u^\infty + u^{corr}, \tag{24}$$

where χ_{Ω^∞} is the indicator function on the patch Ω^∞ (not to be confused with Ω_∞ from section 3),

$$\chi_{\Omega^\infty}(x) := \begin{cases} 1, & x \in \Omega^\infty \\ 0, & \text{else.} \end{cases}$$

The other aspects of the subtraction source model remain unchanged.
The restriction of u^∞ can be justified by two reasons: Firstly, the singularity potential (and its gradient) falls of rapidly with increasing distance to the source, until it is almost zero (cf. (22) figure 1). Secondly, everything we "cut off" is in fact not lost, but can be recovered by the correction potential.

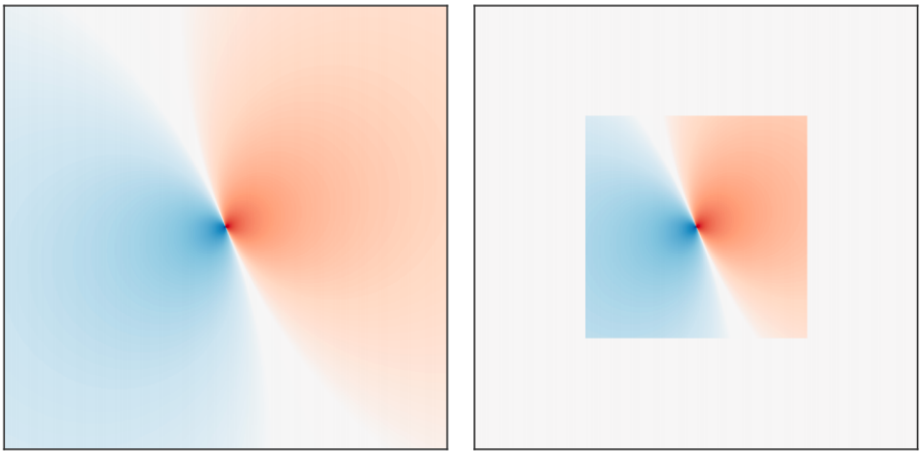

Figure 1: Singularity potential u^∞ (left) and its restriction χ_{Ω^∞} on a square-shaped patch. A blue color indicates negative values and a red color indicates positive values. The colormap is scaled logarithimically towards zero. (Source: Nüßing [8])

The construction and size of the patch will be explained and studied numerically in section 5. Figure 2 shows a schematic representation of a patch. The square shape in figures 1 and 2 indicate hexahedral finite elements, but any kind of polytopes can be used. Note that the patch Ω^∞ can include areas with different conductivities (contrary to Ω_∞).
Naturally, we expect the results of the localized subtraction source model to converge against the results of the subtraction source model with increasing patch size. However, because of the second reason mentioned above, the localized subtraction source model is fundamentally not less accurate than its ancestor.

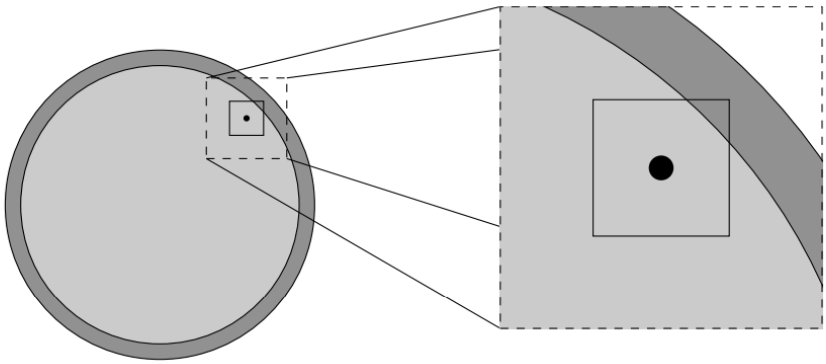

Figure 2: Schematic representation of a square-shaped patch Ω^∞ in relation to Ω. The black dot indicates the dipole position. (Source: Nüßing [8])

In its original formulation from A. Nüßing [8], the localized subtraction source model does not fit into the framework of the CG-FEM. The indicator function is discontinuous while we require the total potential to be continuous. Thus the correction potential will have an opposing discontinuity on the boundary of the patch to make up for the discontinuity of $\chi_{\Omega^\infty} u^\infty$. The discontinuity of u^{corr} can not be represented in the CG finite element space. Consequently, A. Nüßing presented the following discontinuous Galerkin formulation which derivation can be looked up in [8]:

Definition 12 (The DG-FEM using the Localized Subtraction Source Model) *The DG-FEM using the localized subtraction source model is to find $u_h^{corr} \in Y_h^1$ such that $a(u_h, v_h) + J(u_h, v_h) = l(v_h)\ \forall v_h \in Y_h^1$, where*

$$a(u_h^{corr}, v_h) := -\int_\Omega \langle \sigma \bigtriangledown u_h^{corr}, \bigtriangledown v_h \rangle \, dx + \int_{\Gamma_h^{int}} \langle \{\sigma \bigtriangledown u_h^{corr}\}, [\![v_h]\!] \rangle + \langle \{\sigma \bigtriangledown v_h\}, [\![u_h^{corr}]\!] \rangle \, ds,$$

$$J(u_h^{corr}, v_h) := -\eta \int_{\Gamma_h^{int}} \frac{\hat{\sigma}_\gamma}{\hat{\boldsymbol{h}}_\gamma} \langle [\![u_h^{corr}]\!], [\![v_h]\!] \rangle,$$

$$l(v_h) := \int_{\Omega^\infty} \langle \sigma^{corr} \bigtriangledown u^\infty, \bigtriangledown v_h \rangle \, dx - \int_{\Gamma_h^{\infty,int}} \langle \{\sigma^{corr} \bigtriangledown u^\infty\}, [\![v_h]\!] \rangle \, ds + \int_{\partial\Omega^\infty} \langle \sigma^\infty \bigtriangledown u^\infty, n \rangle v_h \, ds$$
$$- \int_{\partial\Omega^\infty} \omega^\infty \langle \sigma \bigtriangledown u^\infty, [\![v_h]\!] \rangle \, ds - \int_{\partial\Omega^\infty} u^\infty \left\langle \{\sigma \bigtriangledown v_h\} - \eta \frac{\hat{\sigma}_\gamma}{\hat{\boldsymbol{h}}_\gamma}, n \right\rangle ds,$$

The interior skeleton of Ω is denoted as Γ_h^{int} and the interior skeleton of Ω^∞ as $\Gamma_h^{\infty,int}$. The weight ω^∞ stands for the average weight on the side of Ω^∞ (cf. 7).

Now the support of the integrals in $l(v_h)$ is only Ω^∞, so the non zero entries of the right-hand side vector l are reduced to #(vertices per element)·#(elements in the patch) non-zero entries.
We see that the DG-FEM formulation is noticeably more complicated than the CG-FEM. More importantly it is computationally more expensive because of the higher dimensional finite element space. In many cases it is not necessary to choose the DG-FEM for its accuracy. Therefore we now adapt the localized subtraction approach to fit a CG-FEM framework.

4.1 A continuous adaptation

In Nüßing's setting, the reason for the discontinuitiy was the indicator function χ_{Ω^∞}. We substitute it with a continuous version $\tilde{\chi}_{\Omega^\infty}$, that has value 1 on the patch, falls off linearly on a transition region $\tilde{\Omega}$ and is zero on the rest $\Omega \backslash (\Omega^\infty \cup \tilde{\Omega})$. The new "indicator function" $\tilde{\chi}_{\Omega^\infty}$ is visualized in figure 3. Here the transition region consists of the elements that touch the patch boundary. Theoretically one could consider choosing a bigger transition region to gain a smoother behaviour of $\tilde{\chi}_{\Omega^\infty} u^\infty$.

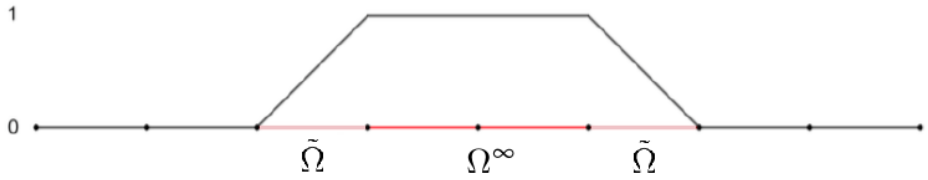

Figure 3: Schematic representation of $\tilde{\chi}_{\Omega^\infty}$.

In the continuous adaptation, the potential u is now written as

$$u = \tilde{\chi}_{\Omega^\infty} u^\infty + u^{corr}. \tag{25}$$

4.1.1 Solving the EEG Forward Problem using the CG-FEM

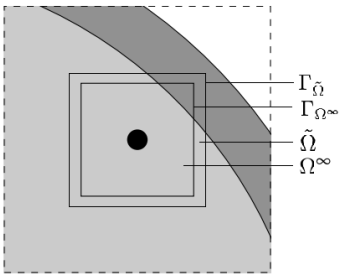

Figure 4: Schematic representation of the patch Ω^∞, the transition region $\tilde{\Omega}$ and their boundaries. (Source: Nüßing [8], modified)

Generally, we want to derive the CG-FEM formulation of the localized subtraction source model in the same way as in section 2.2 and 3.1. For better clarity we first devide the domain Ω into the subdomains Ω^∞ (the patch), $\tilde{\Omega}$ (the transition region) and $\hat{\Omega} := \Omega \backslash (\Omega^\infty \cup \tilde{\Omega})$ (the rest). We also introduce the following notations that are visualized in figure 4[2]:

$$\Gamma_{\Omega^\infty} := \partial\Omega^\infty \cap \partial\tilde{\Omega}, \tag{26}$$

$$\Gamma_{\tilde{\Omega}} := \partial\tilde{\Omega} \cap \partial\hat{\Omega}. \tag{27}$$

We start with the patch Ω^∞. Here $\tilde{\chi}_{\Omega^\infty} \equiv 1$, so the conditions for u are the same as in the subtraction approach. We multiply the Poisson equation from definition 1 with a test function $v_h \in X_h^1$ and integrate over Ω^∞. Then we split the potential and the conductivity to cancel the source term f.

$$\begin{aligned}
\int_{\Omega^\infty} f v_h \, dx &= \int_{\Omega^\infty} \nabla \cdot (\sigma \ \nabla u_h) v_h \, dx \\
&= \int_{\Omega^\infty} \nabla \cdot (\sigma \ \nabla u_h^\infty) v_h \, dx + \int_{\Omega^\infty} \nabla \cdot (\sigma \ \nabla u_h^{corr}) v_h \, dx \\
&= \int_{\Omega^\infty} \underbrace{\nabla \cdot (\sigma^\infty \ \nabla u^\infty)}_{\overset{(21)}{=} f} v_h \, dx + \int_{\Omega^\infty} \nabla \cdot (\sigma^{corr} \ \nabla u_h^\infty) v_h \, dx + \int_{\Omega^\infty} \nabla \cdot (\sigma \ \nabla u_h^{corr}) v_h \, dx.
\end{aligned}$$

[2] If the patch is big enough, it is theoretically possible that Γ_{Ω^∞} and $\Gamma_{\tilde{\Omega}}$ intersect with the outer domain boundary. This is not taken into consideration in the notation of the following calculations. Numerical tests have shown that a patch constructed by two vertex extensions is sufficient. As there are at least three layers between the brain and the outer domain boundary, an intersection of the boundaries does not occur.

After canceling the source term we are left with

$$\int_{\Omega^\infty} \nabla \cdot (\sigma \ \nabla u_h^{corr}) v_h \, dx = - \int_{\Omega^\infty} \nabla \cdot (\sigma^{corr} \ \nabla u^\infty) v_h \, dx.$$

Now we apply Gauss theorem to both sides. The left-hand side becomes

$$\int_{\Omega^\infty} \nabla \cdot (\sigma \ \nabla u_h^{corr}) v_h \, dx \overset{\text{Gauss}}{=} - \int_{\Omega^\infty} \langle \sigma \nabla u_h^{corr}, \nabla v_h \rangle \, dx + \int_{\partial\Omega^\infty} \langle \sigma \nabla u_h^{corr}, n \rangle \, v_h \, ds,$$

and the right-hand side becomes

$$- \int_{\Omega^\infty} \nabla \cdot (\sigma^{corr} \ \nabla u^\infty) v_h \, dx \overset{\text{Gauss}}{=} \int_{\Omega^\infty} \langle \sigma^{corr} \nabla u^\infty, \nabla v_h \rangle \, dx - \int_{\partial\Omega^\infty} \langle \sigma^{corr} \nabla u^\infty, n \rangle \, v_h \, ds$$

Next we add $\int_{\partial\Omega^\infty} \langle \sigma \nabla u^\infty, n \rangle \, v_h \ ds$ to both sides (to cancel the term $\dagger^1$ later). The final left- and right-hand side for the patch are

$$\begin{aligned} LHS(\Omega^\infty) &= - \int_{\Omega^\infty} \langle \sigma \nabla u_h^{corr}, \nabla v_h \rangle \, dx + \underbrace{\int_{\Gamma_{\Omega^\infty}} \langle \sigma \nabla u_h, n \rangle \, v_h \, ds}_{\dagger^1}, \\ RHS(\Omega^\infty) &= \int_{\Omega^\infty} \langle \sigma^{corr} \nabla u^\infty, \nabla v_h \rangle \, dx + \int_{\Gamma_{\Omega^\infty}} \langle \sigma^\infty \nabla u^\infty, n \rangle \, v_h \, ds. \end{aligned}$$

Next, we treat the transition region $\tilde{\Omega}$. Because the source is a point dipole inside the patch, we have $f \equiv 0$ outside of Ω^∞. Therefore the right-hand side is zero.

$$RHS(\tilde{\Omega}) = 0$$

For the left-hand side, we apply the same steps as before, namely multiplying with v_h, integrating and using Gauss theorem:

$$LHS(\tilde{\Omega}) = \int_{\tilde{\Omega}} \nabla \cdot (\sigma \ \nabla u_h) v_h \, dx \overset{\text{Gauss}}{=} - \int_{\tilde{\Omega}} \langle \sigma \nabla u_h, \nabla v_h \rangle \, dx + \int_{\partial\tilde{\Omega}} \langle \sigma \nabla u_h, n \rangle \, v_h \, ds.$$

The boundary of $\tilde{\Omega}$ consists of two parts, that are Γ_{Ω^∞} and $\Gamma_{\tilde{\Omega}}$ (cf. (26). (27)), so we get

$$LHS(\tilde{\Omega}) = - \int_{\tilde{\Omega}} \langle \sigma \nabla u, \nabla v_h \rangle \, dx - \int_{\Gamma_{\Omega^\infty}} \langle \sigma \nabla u_h, n \rangle \, v_h \, ds + \int_{\Gamma_{\tilde{\Omega}}} \langle \sigma \nabla u_h, n \rangle \, v_h \, ds.$$

Note that we switched the sign for the first boundary integral, as n is the unit vector that points outwards of the domain Ω, which is inwards of $\tilde{\Omega}$ in relation to Γ_{Ω^∞}.
Now we split u, but this time $\tilde{\chi}_{\Omega^\infty} \not\equiv 1$, so

$$\begin{aligned} LHS(\tilde{\Omega}) \overset{(25)}{=} &- \int_{\tilde{\Omega}} \langle \sigma \nabla u_h^{corr}, \nabla v_h \rangle \, dx - \int_{\tilde{\Omega}} \langle \sigma \nabla (\tilde{\chi} u^\infty), \nabla v_h \rangle \, dx \\ &- \int_{\Gamma_{\Omega^\infty}} \langle \sigma \nabla u_h, n \rangle \, v_h \, ds + \int_{\Gamma_{\tilde{\Omega}}} \langle \sigma \nabla u_h, n \rangle \, v_h \, ds. \end{aligned}$$

Finally we bring the integral that does not contain the correction potential to the right-hand side. The left- and right-hand side for the transition region then are

$$LHS(\tilde{\Omega}) = -\int_{\tilde{\Omega}} \langle \sigma \bigtriangledown u_h^{corr}, \bigtriangledown v_h \rangle \, dx - \underbrace{\int_{\Gamma_{\Omega^\infty}} \langle \sigma \bigtriangledown u_h, n \rangle \, v_h \, ds}_{\dagger^2} + \underbrace{\int_{\Gamma_{\tilde{\Omega}}} \langle \sigma \bigtriangledown u_h, n \rangle \, v_h \, ds}_{\dagger^3},$$

$$RHS(\hat{\Omega}) = \int_{\tilde{\Omega}} \langle \sigma \bigtriangledown (\hat{\chi} u^\infty), \bigtriangledown v_h \rangle \, dx.$$

At last we look at $\hat{\Omega}$. Again we have $f \equiv 0$, so

$$RHS(\hat{\Omega}) = 0.$$

For the left-hand side, we apply the same steps as for $\tilde{\Omega}$, but without splitting u yet.

$$\begin{aligned} LHS(\hat{\Omega}) &= \int_{\hat{\Omega}} \bigtriangledown \cdot (\sigma \ \bigtriangledown u_h) v_h \, dx \\ &= -\int_{\hat{\Omega}} \langle \sigma \bigtriangledown u_h, \bigtriangledown v_h \rangle \, dx + \int_{\partial\hat{\Omega}} + \langle \sigma \bigtriangledown u_h, n \rangle \, v_h \, ds \\ &= -\int_{\hat{\Omega}} \langle \sigma \bigtriangledown u_h, \bigtriangledown v_h \rangle \, dx - \int_{\Gamma_{\hat{\Omega}}} \langle \sigma \bigtriangledown u_h, n \rangle \, v_h \, ds + \int_{\partial\Omega} \langle \sigma \bigtriangledown u_h, n \rangle \, v_h \, ds \end{aligned}$$

The last integral is zero because of the Neumann boundary condition. Now we only split u in the boundary integral on the left-hand side (we want to cancel the boundary term). On $\hat{\Omega}$ the indicator $\tilde{\chi}_{\Omega^\infty}$ is zero, so we plug in $u = u^{corr}$. The final left- and right hand side for $\hat{\Omega}$ are

$$LHS(\hat{\Omega}) = -\int_{\hat{\Omega}} \langle \sigma \bigtriangledown u_h^{corr}, \bigtriangledown v_h \rangle \, dx - \underbrace{\int_{\Gamma_{\hat{\Omega}}} \langle \sigma \bigtriangledown u_h, n \rangle \, v_h \, ds}_{\dagger^4}$$

$$RHS(\tilde{\Omega}) = 0$$

Eventually, we add all the left- and right hand sides to obtain the whole domain Ω. The marked integrals disappear as $\dagger^1$ cancels with $\dagger^2$ and $\dagger^3$ cancels with $\dagger^4$.

The sums of the left- and right-hand sides are

$$\begin{aligned} LHS(\Omega) &= -\int_{\Omega} \langle \sigma \bigtriangledown u_h^{corr}, \bigtriangledown v_h \rangle \, dx, \\ RHS(\Omega) &= \int_{\Omega^\infty} \langle \sigma^{corr} \bigtriangledown u^\infty, \bigtriangledown v_h \rangle \, dx + \int_{\delta\Omega^\infty} \langle \sigma^\infty \bigtriangledown u^\infty, n \rangle \, v_h \, ds \\ &\quad + \int_{\tilde{\Omega}} \langle \sigma \bigtriangledown (\hat{\chi} u^\infty), \bigtriangledown v_h \rangle \, dx. \end{aligned}$$

We define the following CG-FEM formulation in terms of (bi-)linear forms:

Definition 13 (The CG-FEM using the Localized Subtraction Source Model) *The CG-FEM using the localized subtraction source model is to find $u_h^{corr} \in X_h^1$ such that $a(u_h^{corr}, v_h) = l(v_h) \ \forall v_h \in X_h^1$, where*

$$\begin{aligned} a(u_h^{corr}, v_h) &:= -\int_{\Omega} \langle \sigma \bigtriangledown u_h^{corr}, \bigtriangledown v_h \rangle \, dx, \\ l(v_h) &:= \int_{\Omega^\infty} \langle \sigma^{corr} \bigtriangledown u^\infty, \bigtriangledown v_h \rangle \, dx + \int_{\partial\Omega^\infty} \langle \sigma^\infty \bigtriangledown u^\infty, n \rangle \, v_h \, ds \\ &\quad + \int_{\tilde{\Omega}} \langle \sigma \bigtriangledown (\hat{\chi} u^\infty), \bigtriangledown v_h \rangle \, dx. \end{aligned}$$

On the right-hand side $l(v_h)$ we have a volume integral over the patch, a boundary integral that describes the flow of the flux into the transition region and a volume integral over the transition region. As $\tilde{\chi}_{\Omega^\infty} u^\infty$ falls off to zero inside of $\tilde{\Omega}$ there is no outer boundary integral for the transition region.
As expected, this formulation would be the same as in the subtraction approach (cf. definition 10) if we substituted Ω^∞ with Ω (in this case $\tilde{\Omega} = \varnothing$).

4.2 A Boundary Approach for Solving the MEG Forward Problem

In section 3.2 we have introduced a boundary approach for calculating the secondary B-field. It was explained why this approach is necessary in case of the subtraction source model. The same reasoning applies to the localized subtraction approach. Let us revise the result: The secondary B-field consists of two contributions,

$$B^s(r) = B^s_{corr}(r) + B^s_\infty,$$

the contribution from the correction potential,

$$B^s_{corr}(r) = -\frac{\mu_0}{4\pi} \int_\Omega \sigma \bigtriangledown u^{corr}(r') \times \frac{r - r'}{|r - r'|^3} d^3r',$$

and the contribution from the infinity potential, that is partially rewritten as a boundary integral,

$$\begin{aligned} B^s_\infty(r) = &- \frac{\mu_0}{4\pi} \int_{\Omega \setminus \Omega_\infty} \sigma \bigtriangledown u^\infty(r') \times \frac{r - r'}{|r - r'|^3} d^3r' \\ &- \frac{\mu_0 \sigma^\infty}{4\pi} \int_{\partial\Omega_\infty} u^\infty \left(n \times \frac{r - r'}{|r - r'|^3} \right) ds. \end{aligned}$$

In the framework of the localized subtraction source model, u^∞ is restricted to the patch Ω^∞, so we insert $u = \tilde{\chi}_{\Omega^\infty} u^\infty + u^{corr}$ into B^s_{inf}:

$$\begin{aligned} B^s_\infty(r) = &- \frac{\mu_0}{4\pi} \int_{\Omega \setminus \Omega_\infty} \sigma \bigtriangledown \tilde{\chi}_{\Omega^\infty} u^\infty(r') \times \frac{r - r'}{|r - r'|^3} d^3r' \\ &- \frac{\mu_0 \sigma^\infty}{4\pi} \int_{\partial\Omega_\infty} \tilde{\chi}_{\Omega^\infty} u^\infty \left(n \times \frac{r - r'}{|r - r'|^3} \right) ds. \end{aligned}$$

As $\tilde{\chi}_{\Omega^\infty}$ is one on the patch Ω^∞, non-zero in the transition region $\tilde{\Omega}$ and zero on the rest, and $\Omega_\infty \subset \Omega^\infty$, we split the integrals accordingly to achieve the final boundary approach.

Definition 14 (The boundary approach using the Localized Subtraction Source Model) *The boundary approach for calculating the secondary B-field B^s using the localized subtraction source model is*

$$B^s(r) = B^s_{corr}(r) + B^s_\infty,$$

where

$$B^s_{corr}(r) = -\frac{\mu_0}{4\pi} \int_\Omega \sigma \bigtriangledown u^{corr}(r') \times \frac{r - r'}{|r - r'|^3} d^3r',$$

and

$$
\begin{aligned}
B^s_\infty(r) = &- \frac{\mu_0}{4\pi} \int_{\tilde{\Omega}} \sigma \bigtriangledown \tilde{\chi}_{\Omega^\infty} u^\infty(r') \times \frac{r - r'}{|r - r'|^3} d^3 r' \\
&- \frac{\mu_0}{4\pi} \int_{\Omega^\infty \setminus \Omega_\infty} \sigma \bigtriangledown u^\infty(r') \times \frac{r - r'}{|r - r'|^3} d^3 r' \\
&- \frac{\mu_0 \sigma^\infty}{4\pi} \int_{\partial\Omega_\infty} u^\infty \left(n \times \frac{r - r'}{|r - r'|^3} \right) ds.
\end{aligned}
$$

Similarly to the right-hand side of the EEG forward problem, the support of the integrals has decreased and we can expect the localized subtraction boundary approach to be faster than in case of the subtraction source model.

In the numerical implementation, we restricted Ω^∞ to contain only elements with the same conductivity and chose $\Omega_\infty = \Omega^\infty$. Therefore B^s_∞ is reduced to

$$
\begin{aligned}
B^s_\infty(r) = &- \frac{\mu_0}{4\pi} \int_{\tilde{\Omega}} \sigma \bigtriangledown \tilde{\chi}_{\Omega^\infty} u^\infty(r') \times \frac{r - r'}{|r - r'|^3} d^3 r' \\
&- \frac{\mu_0 \sigma^\infty}{4\pi} \int_{\partial\Omega_\infty} \tilde{\chi}_{\Omega^\infty} u^\infty \left(n \times \frac{r - r'}{|r - r'|^3} \right) ds.
\end{aligned}
$$

In this case the transition region is an extension of the restricted patch, not of the original patch.

5 Validation Studies

In this chapter we inverstigate the numerical integration order and the size of the patch for the localized subtraction source model. Then we compare the CG-FEM localized subtraction approach to other source models, in particular to the subtraction approach. We examine the results of the EEG and MEG forward problem. For the MEG forward problem we use the boundary approach (REF).
The new methods were implemented in the software toolbox *duneuro*[3][9] and the transfer matrix approach was used. A short instruction of how to use the Python interface of *duneuro* and a summary of the parameters can be found in appendix 3.

Head Model

The tests were carried out in a four-layer homogeneous spherical head model consisting of 4876015 tetrahedral elements (786637 nodes). The four layers of the model are: brain, cerebrospinal fluid (CSF), skull and skin. Figure 5 shows a schematic representation of the four layers with the corresponding parameters (radii, conductivities).

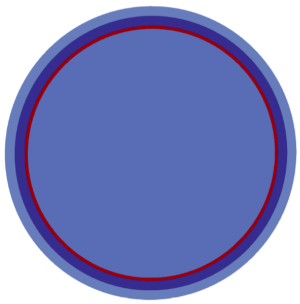

Layer	Outer radius	Conductivity
Brain	78 mm	0.33 S/m
CSF	80 mm	1.79 S/m
Skull	86 mm	0.01 S/m
Skin	92 mm	0.43 S/m

Figure 5: Four-layer spherical head model. Layers starting from the center of the sphere: Brain, CSF, skull, skin.

Sources

In this chapter we study different sets of source dipoles. Every set contains 900 dipoles with unit strength. Each 100 dipoles are placed at the same distance from the center of the sphere and then uniformly distributed at this radius. The radius is chosen so that the dipoles are located inside the brain compartment. The relative distance to the next conductivity jump (here the CSF compartment) is defined as the eccentricity of the dipole. An eccentricity of 0 corresponds to a source located at the center of the sphere and an eccentricity of 1 to a source at the surface between the brain and CSF compartment.
The sets of dipoles that we used are:

- tangentially oriented at eccentricity $0.1 - 0.9$
- radially oriented at eccentricity $0.1 - 0.9$
- tangentially oriented at high eccentricity $0.9 - 0.995$
- radially oriented at high eccentricity $0.9 - 0.995$

The sets that contain radially oriented dipoles were not used for the MEG tests, because in a spherical model radial components do not produce a MEG signal.

Electrodes and Sensors

We used 70 approximately uniformly distributed electrodes on the outer surface of the sphere for the EEG.
For the MEG 240 sensors were placed at a radius of 110 mm outside of the sphere. All three cartesian

[3] www.duneuro.org

components were considered for the orientation of the sensors.

Error Measures

In a homogeneous spherical model we can calculate an analytical solution for the EEG and MEG forward problem [3][12]. The analytical solution serves as a reference for comparing the numerical solutions. We define two error measures, the *relative difference measure* (RDM) and the *magnitude error* (MAG).

Definition 15 (The relative difference measure (RDM)) *The relative difference measure of the analytical solution u_{ana} and a numerical solution u_{num} is defined as*

$$RDM(u_{num}, u_{ana}) := 50 \left\| \frac{u_{num}}{\|u_{num}\|_2} - \frac{u_{ana}}{\|u_{ana}\|_2} \right\|_2 \%.$$

Definition 16 (The magnitude error (MAG)) *The magnitude error of the analytical solution u_{ana} and a numerical solution u_{num} is defined as*

$$MAG(u_{num}, u_{ana}) := 100 \left\| \frac{\|u_{num}\|_2}{\|u_{ana}\|_2} - 1 \right\|_2 \%.$$

The RDM can reach values between 0% and 100%. The optimal error would be 0%. The MAG can have values between −100% and 100%, also with the optimum at 0%.

Boxplots

The RDM and MAG errors are calculated for each dipole in a dipole set. For each 100 dipoles at a fixed eccentricity a statistical analysis is visualized via a boxplot. The colored box shows the interquartile range. The median is represented by a horizontal line inside of the box. The whiskers extending from the box indicate the total range of the errors.

5.1 Integration Order and Patch Size

In *duneuro* the integrals are calculated using a quadrature rule that is based on Gaussian quadrature using Legendre points [11]. The integration order determines the number of one-dimensional quadrature points. The more quadrature points, the higher the degree of polynomials can be for the integration to be exact. In [5] it is shown that for the subtraction source model an integration order of two is necessary and sufficient for tetrahedral meshes. In case of the localized subtraction source model the degree of the integrand is increased by the multiplication with $\tilde{\chi}_{\Omega^\infty}$. Also, the boundary of the patch is closer to the source than the outer domain boundary. Therefore a higher integration order is probably necessary.
When implementing the localized subtraction approach, we need to construct the patch Ω^∞. We start at the dipole element and extend the patch by appending elements that share a vertex with an element of the patch. This step can be done several times. Afterwards another layer is added that will become the transition region (this last extension is not counted when stating the amount of vertex extension). Figure 6 shows an example of a patch visualized with ParaView[4].

To study the integration order, we started with a fixed patch size of two vertex extension, because this was shown to be sufficient in Nüßing's case [8]. First, we tested integration orders of 2-7 and 20.
For the dipole sets with eccentricities 0.1-0-9 we observe that an integration order of 4 is sufficient (see figure 7). Both for RDM and MAG the integration orders 4-20 are visually indistinguishable, while the lower order are less accurate. Especially for the MAG an order of 4 is desirable, as we get visibly worse results for order 2 and 3.

We also tested the sets of dipoles with eccentricities 0.9-0-995 (see figure 8). Below an eccentricity of 0.99 we see a similar trend as in figure 7. However, for the highest eccentricity 0.995, the errors get extremely large when choosing an integration order below 4, but also noticeably for order 5-7. This observation is especially true for the RDM for radial dipoles (lower left corner of figure 8). For the chosen integration orders only the highest order of 20 leads to errors that are in range of the errors at lower eccentricities.

[4] https://www.paraview.org

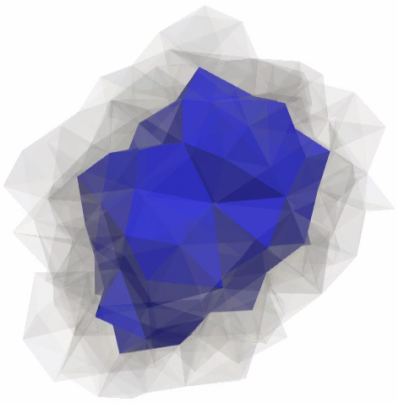

Figure 6: A patch created by two vertex extension. The blue elements are part of the actual patch Ω^{∞} and the grey elements form the transition region $\tilde{\Omega}$.

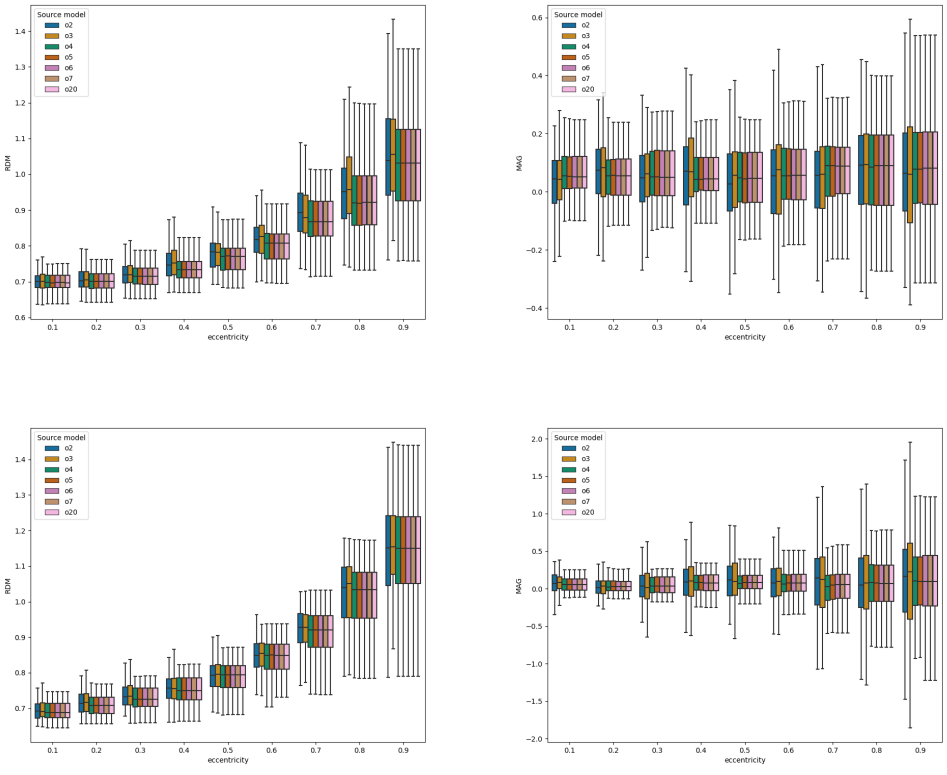

Figure 7: Accuracy comparison for different integration orders. Visualized are the means of the RDM% (first column) and the MAG% (second column) for tangentially (first row) and radially (second row) oriented dipoles at different eccentricities.

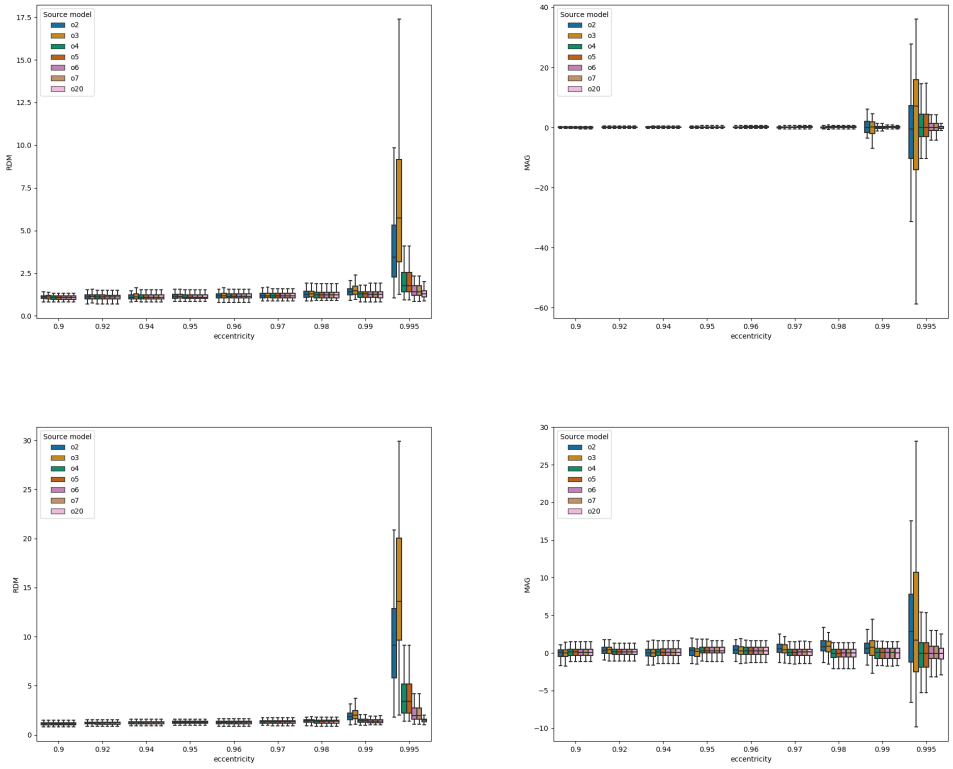

Figure 8: Accuracy comparison for different integration orders. Visualized are the means of the RDM% (first column) and the MAG% (second column) for tangentially (first row) and radially (second row) oriented dipoles at high eccentricities.

To see whether an integration order lower than 20 would already lead to similar results, we tested integration orders 8, 9, 10, 11, 12 and 13 versus order 20. We now only looked at the RDM for radial dipoles at eccentricity 0.995, where the difference was the most relevant (see figure 9). The boxplots show a noticeable decrease of the RDM from order 8 to 10. Starting from order 10 the boxplots are almost the same except for slightly lower medians and a more centered distribution.
We conclude that an integration order of 4 is sufficient for dipoles at eccentricities lower than 0.99, while an integration order above ten is needed for eccentricities higher than 0.99. During the experiments no significant time increase was noticed between choosing integration order 4 or 20. This is because, with two vertex extensions, the patch still consists of relatively few elements. Thus we can afford using a high integration order and chose order 12 for the rest of the experiments.

Next we investigated the effect of the patch size. The tests were performed for 1,2,3 and 4 patch extensions[5]. The patch sizes perform almost equally well. Only the smallest patch produces higher MAG errors for high eccentricities (see figure 11). Therefore we stick to the choice of two vertex extensions. This fits the observations of A. Nüßing [8][6].

5.2 Accuracy Comparison of EEG Forward Results

After having set the parameters for the localized subtraction (LSUB) source model we want to compare it to other source models, namely the partial intergration[7] (PI), Venant (VEN) and especially the subtraction (SUB) source model.

For low eccentricities the VEN, SUB and LSUB show similar accuracy (see figure 12). The SUB is more

[5]Zero patch extensions have been tested as well which leads to very high errors even when using an integration order of 20. The errors are not presented in the figures as they are out of scale.
[6]He has also shown that the error curve for more than one extension is smoother than for the smallest patchsize.
[7]It is well known that the PI is less accurate than the other approaches. It is only shown as a reference size and will not be discussed.

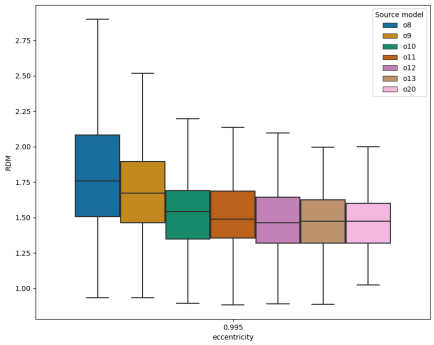

Figure 9: Accuracy comparison for different integration orders. Visualized are the means of the RDM% (first column) and the MAG% (second column) for tangentially (first row) and radially (second row) oriented dipoles at high eccentricities.

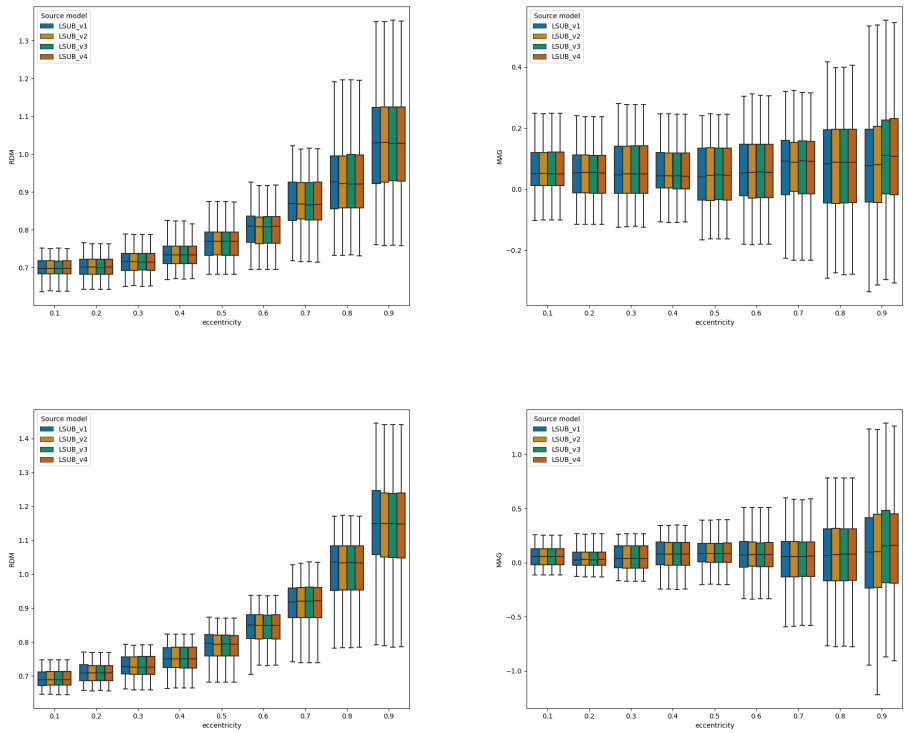

Figure 10: Accuracy comparison of varying amount of vertex extensions for the localized subtraction source model (LSUB). The suffix _v2 indicates two vertex extensions, _v3 three vertex extensions etc.. Visualized are the means of the RDM% (first column) and the MAG% (second column) for tangentially (first row) and radially (second row) oriented dipoles at high eccentricities.

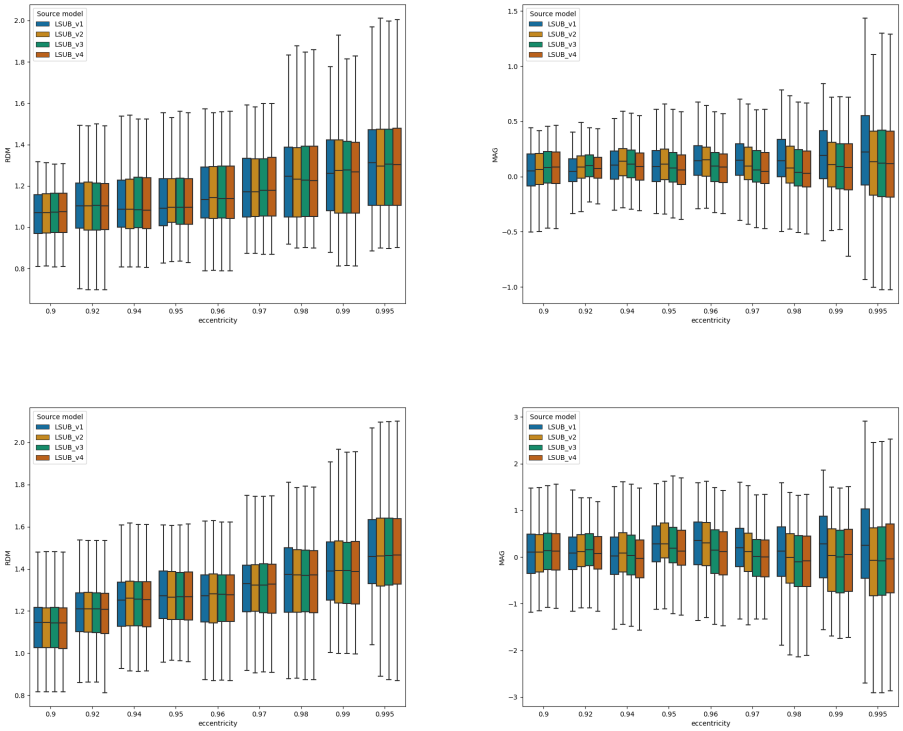

Figure 11: Accuracy comparison of varying amount of vertex extensions for the localized subtraction source model (LSUB). The suffix _v2 indicates two vertex extensions, _v3 three vertex extensions etc.. Visualized are the means of the RDM% (first column) and the MAG% (second column) for tangentially (first row) and radially (second row) oriented dipoles at high eccentricities.

accurate than the VEN, except when reaching an eccentricity of 0.9. The LSUB even performs slightly better than the SUB, especially at a higher eccentricity of 0.9 where it is is also better than the VEN.
For high eccentricities 0.9-0.995 these observations are reinforced (see figure 13). For the RDM the accuracy of the SUB gets increasingly worse until reaching a median of ≈ 2% for tangential and ≈ 3.5% for radial sources. The total range reaches 4% and 7% respectively. Meanwhile the RDM for the VEN only slightly increases, with a total range staying under 2% for tangential and under 3 % for radial sources. The RDM of the LSUB is almost identical to the VEN in case of tangential sources, but is clearly more accurate in case of radial sources.
Similar observations can be made for the MAG error. For tangential orientations the subtraction suddenly reaches a maximum error of 15% at the highest eccentricity, whereas the VEN and LSUB consistently stay under 3%.
For radial orientations, the SUB again gets increasingly less accurate with a maximum error of almost 7%. The VEN loses 2% of accuracy for eccentricities higher than 0.98 and reaches a maximum MAG error of ≈ - 4%. The LSUB clearly peforms the best, with medians close to zero and a total range error of less than 3%, consistenly across all eccentricities.

Generally, one could say that the VEN and SUB perform similarly well, except for the SUB resulting in increasingly larger errors for eccentricities higher than 0.9. This behaviour of the SUB is already well known and was theoretically explained by convergence analysis [15]. The LSUB overall performs similarly to the VEN, but with even better results for radial sources at high eccentricities.

5.3 The Boundary Approach for calculating the Secondary B-field

The boundary approach demands a construction of the region Ω_∞. For both the SUB and the LSUB Ω_∞ was constructed in the same way as the patch Ω^∞ for the LSUB. Two vertex extensions were used, but this time, the patch was restricted to the brain compartment, meaning only elements were added that have the same conductivity as the dipole element. This was necessary for proposition 1. For the boundary integral over the surface of Ω_∞, an integration order of 12 was used.

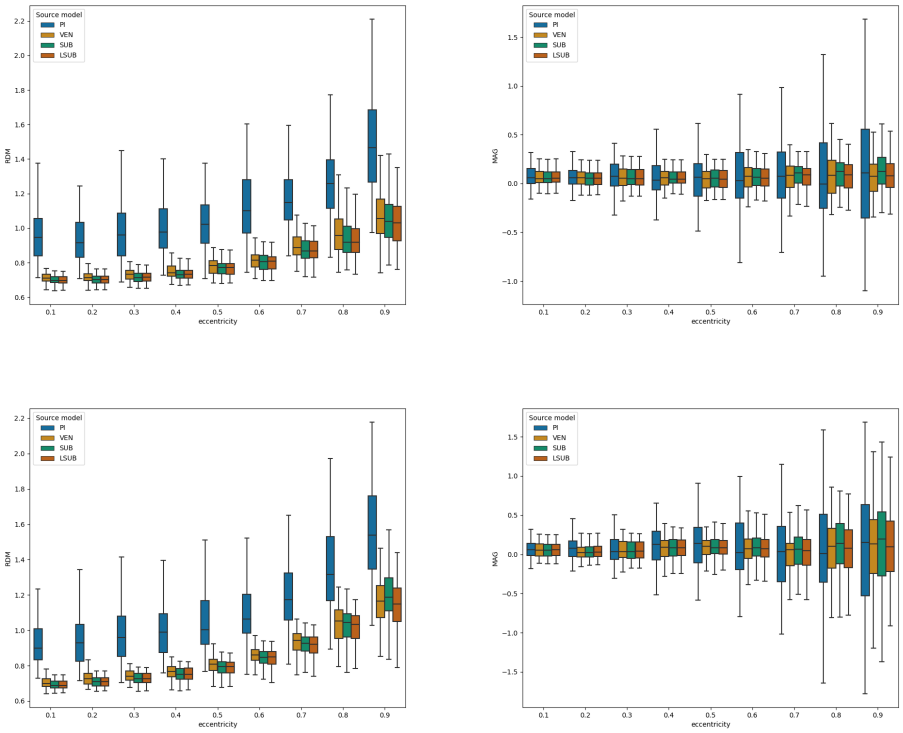

Figure 12: Accuracy comparison for the EEG of different source models: Partial Integration (PI), Venant (VEN), Subtraction (SUB) and Localized Subtraction (LSUB). Visualized are the RDM% (first column) and the MAG% (second column) for tangentially (first row) and radially (second row) oriented dipoles at different eccentricities.

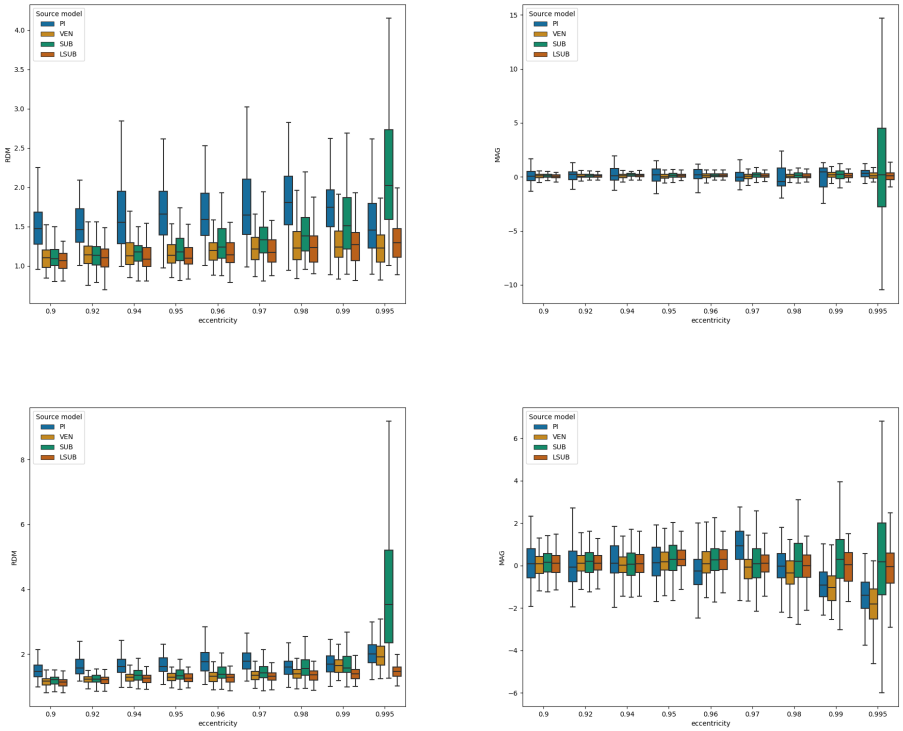

Figure 13: Accuracy comparison for the EEG of different source models: Partial Integration (PI), Venant (VEN), Subtraction (SUB) and Localized Subtraction (LSUB). Visualized are the RDM% (first column) and the MAG% (second column) for tangentially (first row) and radially (second row) oriented dipoles at high eccentricities.

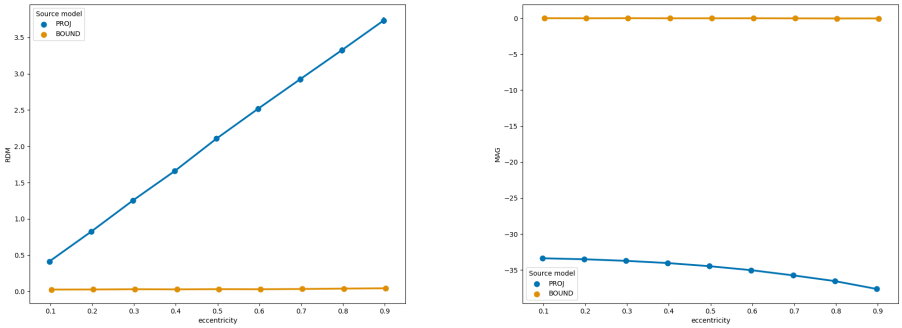

Figure 14: Comparison between the projected (PROJ) and the boundary (BOUND) approach to calculate the secondary B-field using the subtraction source model. Visualized are the means of the RDM% (first column) and the MAG% (second column) for tangentially oriented dipoles.

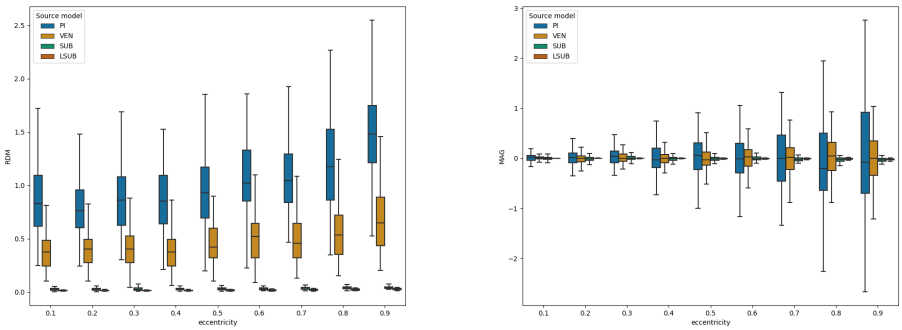

Figure 15: Accuracy comparison for the secondary B-field of different source models: Partial Integration (PI), Venant (VEN), Subtraction (SUB) and Localized Subtraction (LSUB). Visualized are the RDM% (first column) and the MAG% (second column) for tangentially oriented dipoles.

At first we want to investigate the advantage of the boundary approach per se. In section 3.2 we have shortly explained that a projection of the singularity potential into the finite element space might lead to approximation errors and thereby motivated the boundary approach. Figure 14 clearly shows that the projected approach leads to huge errors, while the boundary approach results in high accuracy.

Next we compare the accuracy of the MEG results for the different source models. At first glance, we can see that the SUB and LSUB are exceedingly accurate for eccentricities 0.1-0.9 (see figures 15 and 16). The VEN performs very well, with errors under 1.5% for both RDM and MAG. But the SUB stays under 0.15% in both cases. The LSUB is even more accurate, with a maximum error of 0.06%.

For higher eccentricities we split the plots in two parts to obtain an informative range of the y-axis, as the errors for the SUB and LSUB explode for eccentricities higher than 0.99.

For eccentricities 0.9-0.98 (see figure 17) we observe a similar behaviour as for the low eccentricities. However the RDM and MAG errors for the SUB suddenly increase between eccentricity 0.97 and 0.98. The increase in errors for the SUB is natural, as the errors of the EEG forward problem also increased for higher eccentricities. Surprisingly, the total range of the SUB is still better than for the VEN, even though the VEN performed better for eccentricities higher than 0.9 for the EEG forward problem.

For very high eccentricities of 0.9 and 0.995 the errors for the SUB explode, surpassing 15% for the RDM and 25% for the MAG (even as high as 125% for for the highest eccentricity). The LSUB still performs well for eccentricity 0.9, but then also reaches huge errors for the highest eccentricity. In case of the RDM the median is almost 20%. In case of the MAG the median is still approximately 5%, but with an interquartile range of more than 40 %.

The sudden increase in errors at eccentricity 0.995 for the LSUB could result from the restriction of the patch. For the boundary approach, we restricted the patch to include only elements with the same conductivity. For the highest eccentricity 0.995, the element containing the dipole is sometimes already touching the CSF and does not further extend. Therefore the boundary integral is calculated very close to

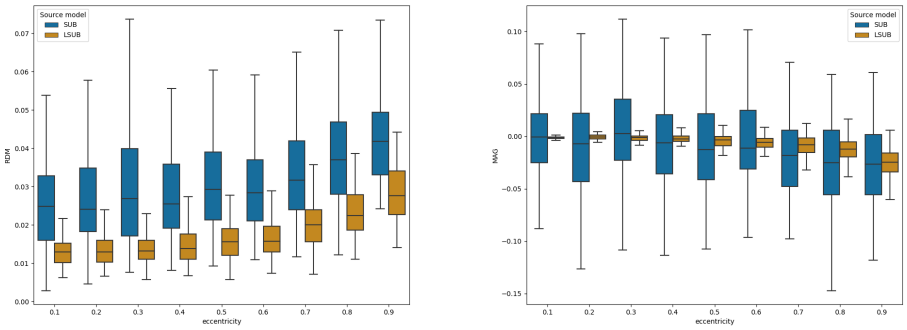

Figure 16: Accuracy comparison for the secondary B-field of the Subtraction (SUB) and Localized Subtraction (LSUB) source model. Visualized are the RDM% (first column) and the MAG% (second column) for tangentially oriented dipoles.

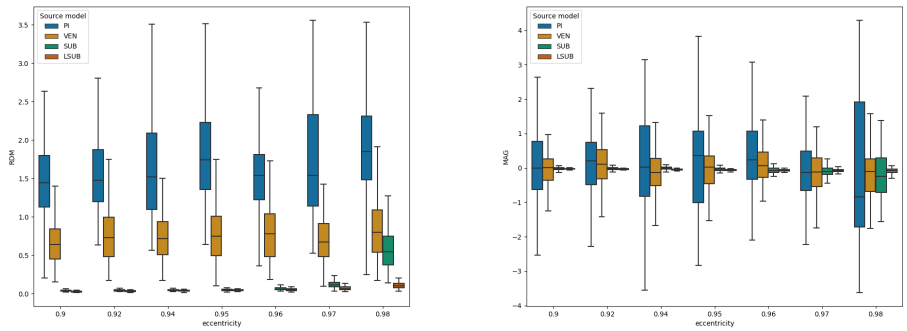

Figure 17: Accuracy comparison for the secondary B-field of the Subtraction (SUB) and Localized Subtraction (LSUB) source model. Visualized are the RDM% (first column) and the MAG% (second column) for tangentially oriented dipoles at eccentricities 0.9-0.98.

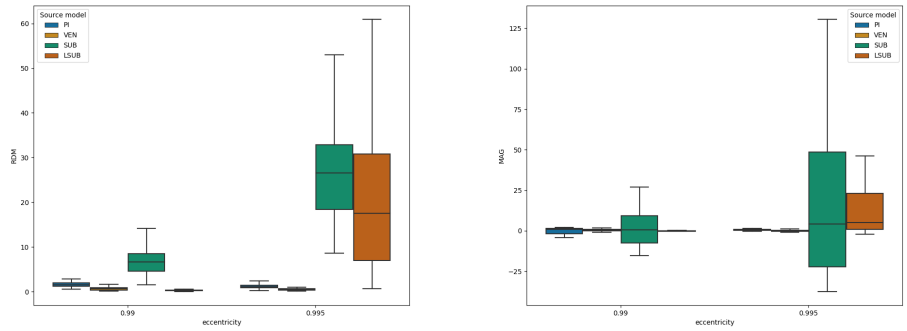

Figure 18: Accuracy comparison for the secondary B-field of the Subtraction (SUB) and Localized Subtraction (LSUB) source model. Visualized are the RDM% (first column) and the MAG% (second column) for tangentially oriented dipoles at eccentricities 0.9 and 0.995.

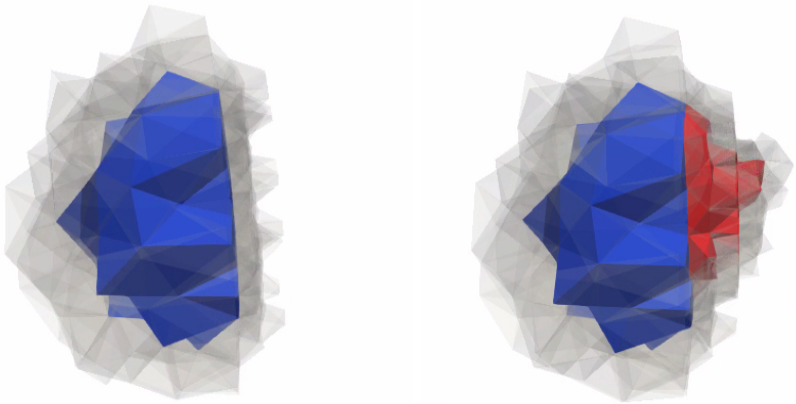

Figure 19: Comparison of a restricted patch (left) and a non-restricted patch (right). The blue elements are contained in the brain compartment and the red elements are contained in the CSF compartment. The dipole in the center of the patch was positioned at an eccentricity of 0.995.

the source position, where the values of the singularity potential change rapidly and the approximation of the quadrature rules gets worse[8]. Figure 19 shows the difference between a restricted and a non-restricted patch at eccentricity 0.995. However, even if we did not restrict the patch Ω^{∞}, we would still have an integral over the boundary of Ω_{∞}. The latter region must be restricted to the brain layer.

To summarize, the SUB and LSUB together with the boundary approach result in a highly accurate calculation of the secondary B-field, except for very high eccentricities. The SUB can be used for eccentricities up to 0.98 and the LSUB can be used up to 0.99.

5.4 Time Efficiency of the Localized Subtraction Source Model

The time consumption for solving the EEG and MEG forward problem can generally be divided into the following steps: Calculating of the transfer matrices, assembling the right-hand side vector l and multiplying l with the transfer matrices. The first step is the same for every source model, but the last two steps scale linearly with the amount of non-zero entries in l. Therefore the SUB has a high time consumption that strongly depends on the total number of elements of the head domain (# non-zero entries = # nodes in Ω). As the LSUB reduced the number of non-zero entries to the nodes in the patch and the transition region, we expect it to be much quicker. For two vertex extensions, the patch consisted of $\approx 200-700$ elements and the transition region consisted of $\approx 800-2000$ elements (depending on the location of the source and the surrounding structure of the mesh). Together we have $\approx 1000-2700$ elements for the LSUB in contrast to the total 4876015 elements of the head model. Also, the amount of elements in the patch and transition region is independent from the total size and resolution of the mesh. For the SUB and LSUB an additional step has to be done after solving the forward problem: Adding the contribution of the singularity potential. This step is called post-processing. For the EEG this means simply adding u^{∞}. For the MEG, this means adding B^s_{∞} from the boundary approach. Again, the amount of points where B^s_{∞} has to be calculated was immensely decreased for the LSUB and we can expect an improvement in comparison to the SUB.

The table in figure 20 shows the mean time consumption for solving the forward problem and MEG post-processing for a single dipole. The means were calculated from 10000 runs with randomly distributed dipoles. The VEN is given as a reference.

As expected, the LSUB has lead to a major speed up. The total time for the EEG and MEG forward calculations decreased from 1056 to 43 ms, or from 1106 to 48 ms, respectively. This is a factor of approximately 24.

The computation for the EEG and MEG forward problem for the LSUB is almost as quick as for the VEN. Knowing that the number of non-zero entries in l for the VEN is the number of nodes in neighbouring elements of the source [10], this result is very plausible.

[8]Integration orders up to 20 did not change the result.

	SUB	LSUB	VEN
EEG total	1056ms	43ms	31ms
MEG (no postproc.)	1106ms	48ms	38ms
MEG postprocessing	637ms	265ms	n.a.
MEG total	1743ms	313ms	38ms

Figure 20: Comparison of computation times.

The additional computational effort for the MEG postprocessing was also reduced by a factor of 2.4, taking 265 ms per dipole.

6 Conclusion

This thesis presented the localized subtraction source model.
After recalling the transfer matrix approach, we noted that source models that result in a sparse right-hand side can immensely reduce calculation time. Next we presented the subtraction source model, which divided the solution into the correction potential and the singularity potential, maintaining the original singular source representation. The subtraction source model is very accurate, but also too slow for practical applications because of its dense right-hand side.
To improve the subtraction approach, the localized subtraction source model was introduced. It maintained the general concept of the subtraction source model, but restricted the singularity potential to a small patch. The restriction resulted in a sparse right-hand side. As the orginal framework of the localized subtraction source model was only fit for a discontinuous finite element framework, we proposed a continuous adaptation and derived a CG-FEM formulation.
Furthermore, we adapted a boundary approach to calculate the secondary B-field, that was originally designed for the subtraction source model. Numerical tests showed that the localized subtraction source model was not less accurate than the subtraction source model. In fact, it performed even better, because a high integration order could be applied. Generally, the localized subtraction source model was the most accurate, except for the MEG forward problem at eccentricities higher than 0.99. Perhaps these errors are preventable by using a higher integration order, not restricting the patch to the brain compartment, or constructing a transition region that consists of more than one vertex extension (to obtain a smoother $\nabla(\tilde{\chi}_{\Omega^\infty} u^\infty)$).
As expected, the localized sbtraction source model achieved a major speed up for the computation time in comparison to the subtraction source model. The computation times for the EEG and MEG forward problem (without post processing) were similar to the Venant source model.
Conclusively, the localized subtraction source model is a significant improvement to the subtraction source model, as it is both slightly more accurate and, more importantly, much quicker.

7 Appendix

Appendix 1 (Proof of lemma 1) We proof that for a vector field F and a scalar field ϕ it holds true that $\nabla \times (\phi F) = \nabla\phi \times F + \phi \nabla \times F$:

$$
\begin{aligned}
\nabla \times (\phi F) &= \begin{pmatrix} \frac{\partial(\phi F_3)}{\partial x_2} - \frac{\partial(\phi F_2)}{\partial x_3} \\ \frac{\partial(\phi F_1)}{\partial x_3} - \frac{\partial(\phi F_3)}{\partial x_1} \\ \frac{\partial(\phi F_2)}{\partial x_1} - \frac{\partial(\phi F_1)}{\partial x_2} \end{pmatrix} \\
&= \begin{pmatrix} \left(\frac{\partial\phi}{\partial x_2} F_3 + \frac{\partial F_3}{\partial x_2}\phi\right) - \left(\frac{\partial\phi}{\partial x_3} F_2 + \frac{\partial F_2}{\partial x_3}\phi\right) \\ \left(\frac{\partial\phi}{\partial x_3} F_1 + \frac{\partial F_1}{\partial x_3}\phi\right) - \left(\frac{\partial\phi}{\partial x_1} F_3 + \frac{\partial F_3}{\partial x_1}\phi\right) \\ \left(\frac{\partial\phi}{\partial x_1} F_2 + \frac{\partial F_2}{\partial x_1}\phi\right) - \left(\frac{\partial\phi}{\partial x_2} F_1 + \frac{\partial F_1}{\partial x_2}\phi\right) \end{pmatrix} \\
&= \begin{pmatrix} \frac{\partial\phi}{\partial x_2} F_3 - \frac{\partial\phi}{\partial x_3} F_2 \\ \frac{\partial\phi}{\partial x_3} F_1 - \frac{\partial\phi}{\partial x_1} F_3 \\ \frac{\partial\phi}{\partial x_1} F_2 - \frac{\partial\phi}{\partial x_2} F_1 \end{pmatrix} - \begin{pmatrix} \frac{\partial F_3}{\partial x_2}\phi - \frac{\partial F_2}{\partial x_3}\phi \\ \frac{\partial F_1}{\partial x_3}\phi - \frac{\partial F_3}{\partial x_1}\phi \\ \frac{\partial F_2}{\partial x_1}\phi - \frac{\partial F_1}{\partial x_2}\phi \end{pmatrix} \\
&= \nabla\phi \times F + \phi \nabla \times F.
\end{aligned}
$$

□

Appendix 2 (Proof of lemma 2) We proof that for a vector field F it holds true that $\int_\Omega \nabla \times F \, dx = \int_{\partial\Omega} n \times F \, ds$:

$$
\int_\Omega \nabla \times F \, dx = \int_\Omega \begin{pmatrix} \frac{\partial}{\partial x_2} F_3 \\ \frac{\partial}{\partial x_3} F_1 \\ \frac{\partial}{\partial x_1} F_2 \end{pmatrix} dx - \int_\Omega \begin{pmatrix} \frac{\partial}{\partial x_3} F_2 \\ \frac{\partial}{\partial x_1} F_3 \\ \frac{\partial}{\partial x_2} F_1 \end{pmatrix} dx
$$

Now we apply the componentwise version of Gauss' theorem, that is $\int_\Omega \frac{\partial}{\partial x_i} F_j = \int_{\partial\Omega} n_i F_j ds$ to each vector entry and obtain

$$
\int_\Omega \nabla \times F \, dx = \int_{\partial\Omega} \begin{pmatrix} n_2 F_3 \\ n_3 F_1 \\ n_1 F_2 \end{pmatrix} ds - \int_{\partial\Omega} \begin{pmatrix} n_3 F_2 \\ n_1 F_3 \\ n_2 F_1 \end{pmatrix} ds = \int_{\partial\Omega} n \times F \, ds.
$$

□

Appendix 3 (Solving the Forward Problem using the duneuro Python interface 'duneuropy')

Step 1: Build the MEEG driver.
The MEEG driver is a python object that creates the volume conductor and can call all relevant functions.

```
driver_configs = {
        'type' : 'fitted',
        'solver_type' : 'cg',                   # continuous Galerkin
        'element_type' : 'tetrahedron',
        'volume_conductor' : {                  # configurations for the volume conductor
                'grid.filename' : 'path.msh',
                'tensors.filename' : 'path.cond'
        },
        'meg' : {                       # configurations for the MEG
                'intorderadd' : 3,              # additional integration order
                'type' : 'physical'             # projection of the flux σ ∇ u into the finite element space
        }
}
driver = duneuropy.MEEGDriver3d(driver_configs)
```

Remark: The actual intergration order is calculated by *intorderadd + 2* order(FE basis functions).*

Step 2: Compute the stiffness and secondary flux integration matrix.
Load the sensor positions and orientations from a text file and convert them into a list of *FieldVector3D*.

```
electrode_configs = {
        'type' : 'closest_subentity_center',
        'codims' : [3]
}

driver.setElectrodes(electrodePositions, electrode_configs)                # EEG sensors
driver.setCoilsAndProjections(coilPositions, coilOrientations)                  # MEG sensors
```

Step 3: Compute the transfer matrices.

```
tm_configs = {
        'solver' : {
                'reduction' : 1e-15                # minimum defect reduction for solving the linear system
        }
}

tm_eeg = driver.computeEEGTransferMatrix(tm_configs)
tm_meg = driver.computeMEGTransferMatrix(tm_configs)
```

Step 4: Apply the transfer matrices

First we define the sources for which we want to compute the solution. We need a list of the dipole positions and the dipole moments. Then we convert them into *duneuropy.Dipole3D* objects.

```
dipoles = [duneuropy.Dipole3D(p,m) for p,m in zip(dipolePositions, dipoleMoments)]
```

Now we apply the transfer matrices.

```
solution_eeg = driver.applyEEGTransfer(tm_eeg, dipoles, tm_configs)
solution_meg = driver.applyMEGTransfer(tm_meg, dipoles, tm_configs)      # not yet multiplied by -μ/4π
```

For this step, the configurations in the last argument must also include the choice of the source model. In case of the subtraction and localized subtraction source model, post processing can be turned on. Note, that when post processing is done for the MEG, it has to be turned off for the EEG.

```
tm_configs = {
        'solver' : {
                'reduction' : 1e-15                # minimum defect reduction for solving the linear system
        },
        'source_model' : source_model_configs,                  # depends on choice of the source model
        'post_process' : False,                # EEG post processing
        'post_process_meg' : True                  # MEG post processing boundary approach
}
```

The source model configurations must be defined for the chosen model. The configurations for the localized subtraction source model are presented here.

```
source_model_configs = {
        'type' : 'localized_subtraction',
        'initialization' : 'single_element',                  # first element of the patch
        'extensions' : ['vertex', 'vertex'],                  # specify amount of vertex extensions
        'restrict' : False,                # restricts the patch to the brain compartment, set true for MEG
        'intorderadd' : 10,                # additional integration order for volume integrals
        'intorderadd_lb' : 10,                # additional integration order for boundary integrals
        'intorder_meg' : 20,                # integration order for MEG post processing volume integrals
        'intorder_meg_lb' : 20                # integration order for MEG post processing boundary integrals
}
```

The last two parameters are only needed for the MEG post processing. The parameters *initialization, extensions* and *restrict* are used for the construction of the patch Ω^{∞}. When using the subtraction approach these parameters need to be defined as well for the construction of Ω_{∞} in the MEG boundary approach. Note that in this case *restrict* must be set to *True.*

8 Sources

[1] D. N. Arnold, F. Brezzi, B. Cockburn, L. D. Marini: *Unified analysis of discontinuous galerkin methods for eppiliptic problems.* SIAM journal on numerical analysis, 39(5):1749-1779, (2016).

[2] D. Braess: *Finite elements: theory, fast solvers and applications in solid mechanics.* Cambridge University Press, 2007.

[3] J. De Munck, M. J. Peters: *A fast method to compute the potential in the multisphere model.* IEEE Trans. Biomed. Eng, 40(11):1166-1174, 1993.

[4] D. A. Di Pietro, A. Ern: *Mathematical aspects of discontinuous Galerin methods*, Volume 69. Springer Science & Business Media. (2011)

[5] F. Drechsler, C. H. Wolters, T. Dierkes, H. Si, L. Grasedyck: *A highly accurate full subtraction approach for finite element based source analysis using constrained Delaunay tetrahedralisation.* NeuroImage, 46(4):1055-11065, 2009.

[6] C. Engwer, J. Vorwerk, J.Ludewig, C. Wolters: *A Discontinuous Galerkin Method to Solve the EEG Forward Problem Using the Subtraction Approach.* SIAM Journal on Scientific Computing, 39(1):B138-B164, 2017.

[7] M. Hämäläinen, R. Hari, R.J. Ilmoniemi, J. Knuutila, O. V. Lounasmaa: *Magnetoencephalography - theory, instrumentation, and applications to noninvasive studies of the working human brain.* Reviews of mordern Physics, 65(2):413, 1993.

[8] A. Nüßing: *Fitted and Unfitted Finite Element Methods for Solving the EEG Forward Problem.* Dissertation, 2018.

[9] A. Nüßing, M. C. Piastra, S. Schrader, T. Miinalainen, H. Brinck, C. H. Wolters, C. Engwer: *duneuro - a software toolbox for forward modelling in neuroscience.* http://arxiv.org/abs/1901.02874.

[10] M. C. Piastra: *New Finite Element Methods for Solving the MEG and the Combined MEG/EEG Forward Problem.* Dissertation, 2019.

[11] A. Quarteroni, R. Sacco, F. Saleri: *Numerical mathematics*, volume 37. Springer Science & Business Media, 2010.

[12] J. Sarvas: *Basic mathematical and electromagnetic concepts of the biomagnetic inverse problem.* Physics in medicine and biology, 32(1):11, 1987.

[13] J. Vorwerk: *New finite element methods to solve the EEG/MEG forward provlem.* Dissertation, 2016.

[14] C. H. Wolters, L. Grasedyck, W. Hackbusch: *Efficient computations of lead field bases and influence matrix for the FEM-based EEG and MEG inverse problem.* Inverse Problems, 20(4):1099, 2004.

[15] C. H. Wolters, H. Köstler, C. Möller, J. Härdtlein, L. Grasedyck, W. Hackbusch: *Numerical mathematics of the subtraction method for the modelling of a current dipole in EEG source reconstruction using finite element head models.* SIAM Journal on Scientific Computing, 30(1):24-45, 2007.

Declaration of Academic Integrity

I hereby confirm that this thesis on "The Localized Subtraction Source Model - For Solving the EEG and MEG Forward Problem using the Continuous Galerkin Finite Element Method" is solely my own work and that I have used no sources or aids other than the ones stated. All passages in my thesis for which other sources, including electronic media, have been used, be it direct quotes or content references, have been acknowledged as such and the sources cited.

I agree to have my thesis checked in order to rule out potential similarities with other works and to have my thesis stored in a database for this purpose.

Münster, December 30, 2021

Pia Lange